PAPER

First theoretical framework of Al_9N_9 and B_9N_9 nanorings for unveiling their unique detection and sensing potential for SF_6 decomposition gases (H_2S, SO_2, SOF_2, and SO_2F_2): toward real-time gas sensing in high-voltage power systems†

Hafiz Ali Rizwan,[a] Muhammad Usman Khan, [ID] *[a] Abida Anwar,[a] Sarah Alharthi[bc] and Mohammed A. Amin[b]

Sulfur hexafluoride (SF_6) is widely used as an insulating gas in high-voltage electrical equipment due to its excellent dielectric properties. However, its decomposition under electrical discharges can generate toxic and corrosive byproducts such as H_2S, SO_2, SOF_2, and SO_2F_2, which pose serious threats to insulation integrity and the reliability of power systems. Rapid and accurate sensing and detection of these decomposition products is thus critical for fault diagnosis and preventative maintenance. Despite various experimental advances, the development of efficient, sensitive, and real-time nanomaterial-based gas sensors remains a challenge. In this study, we systematically investigate the sensing capabilities of Al_9N_9 (AlN) and B_9N_9 (BN) nanorings for SF_6 decomposition gases using density functional theory (DFT) with the B3LYP-D3/6-31G(d,p) method. Different key electronic and structural evaluations including adsorption energy (E_{ads}) measurements, energy gap (E_g) determinations, natural bond orbital (NBO), density of states (DOS), thermodynamic studies, atom in molecules (AIM), non-covalent interactions (NCI) and sensing mechanism were carried out to assess the sensing performance. The adsorption of these gases on AlN nanoring results in higher adsorption energies ranging from -8.690 kcal mol^{-1} to -38.221 kcal mol^{-1} while these gases are weakly adsorbed on BN nanorings (-7.041 to -7.855 kcal mol^{-1}). The reduction of the energy gap is observed after the adsorption of SF_6 decomposed gases on both rings. The most notable reduction is observed after the adsorption of SO_2 on AlN (1.103 eV) and BN (2.883 eV) nanorings. The study demonstrated that SO_2 showed maximum sensitivity on BN nanorings (0.9797), accompanied by a substantial work function increase of 36.715% which confirmed BN as the most reactive material for SO_2 detection. The adsorption of SF_6 on AlN and BN nanorings produced fast recovery times, which shows their potential for real-time sensor applications, with the increase in temperature further decreasing the recovery time. Both AlN and BN nanorings showed better detection performance for SO_2, while AlN nanorings proved more efficient for SOF_2 and SO_2F_2 detection because of their superior electrical conductivity, better charge transfer, and quicker recovery times. These findings recommend the integration of Al_9N_9 and B_9N_9 nanorings in advanced gas sensor technologies for real-time, reliable detection of SF_6 decomposition gases, crucial for enhancing the safety and efficiency of high-voltage power systems.

[a]Department of Chemistry, University of Okara, Okara-56300, Pakistan. E-mail: usman.chemistry@gmail.com; usmankhan@uo.edu.pk

[b]Department of Chemistry, College of Science, Taif University, Taif 21944, Saudi Arabia

[c]Research Center of Basic Sciences, Engineering and High Altitude, Taif University, Taif 21944, Saudi Arabia

† Electronic supplementary information (ESI) available. See DOI: https://doi.org/10.1039/d5ra03312h

1. Introduction

Sulphur hexafluoride (SF_6) is a widely used gas in the electrical power sector due to its high dielectric strength, thermal stability, and ability to quench electrical arcs.[1–4] As a dielectric medium in gas-insulated switchgear (GIS), circuit breakers, transformers, and high-voltage power transmissions, it guarantees safe operation and efficiency.[5–7] SF_6 is capable of breaking down at high electrical discharges and at partial breakdown conditions to yield several toxic and corrosive byproducts such as H_2S, SO_2, SOF_2, and SO_2F_2.[7,8] These

decomposition products are very dangerous to electrical personnel because when the decomposition products corrode components of the insulation of a variety of equipment, degradation is experienced, which in turn reduces the life and reliability of the equipment.[9–11] Therefore, the early and accurate identification of these gases is essential to monitor insulation points and avoid equipment defects and risks to work and life.[12]

In recent years, nanomaterials have attracted extensive attention in the field of gas sensing attributable to their exceptional physicochemical properties, including large surface area, adjustable electronic structures, and excellent molecule adsorption capacity.[13–15] These composite structures provided the structure with abundant active sites for gas adsorption, which improved the capacity and selectivity of sensors.[16,17] These unique features may be useful for optical devices,[18,19] catalysis,[20] sensing materials (sensors),[21] adsorption processes,[22] medicinal therapies,[23] and electronic devices[24] since Kroto et al. synthesized the C_{60} carbon fullerene.[25,26]

In this context, carbonaceous nanomaterials including the recent graphene, carbon nanotubes (CNT), and fullerene derivatives are being used for gas-sensing properties due to the high electron mobilities and high surface-to-volume ratios.[27,28] Nevertheless, pure CNT is not very useful for gas sensing since it has a weak reaction and is not very sensitive to gas molecules.[29,30] The ability of pure graphene to detect some gas molecules, as H_2, CO_2, NO, NO_2, CO, and NH_3, is similarly diminished due to its very low sensitivity to these molecules.[31,32] Graphene quantum dots and graphene nanoribbons are two other carbon allotropes that have been studied for gas detection. However, the findings also indicate that these materials exhibit poor interactions with gas molecules in their pure forms.[33,34] The previous discussion makes it clear that pure carbon-based nanomaterials are not suited for developing better nano-sensors because they interact poorly with gas molecules.[35]

Additionally, several group III nitrides have been studied both experimentally and theoretically.[36,37] However, boron and aluminium nitrides stand out for their exceptional physical and chemical characteristics, making them the favoured options. Interactions between NH_3 molecules and aluminium nitride and boron nitride nanotubes are more substantial than those between CNTs and NH_3 molecules.[38–40] Also, $B_{12}N_{12}$ fullerene is great at detecting NH_3 gas but isn't ideal for CO and NO gas.[40] Material with Fe, Co, Ni, Cu, and Zn metals on $Al_{12}N_{12}$ nanoclusters were efficiently designed for hydrogen storage by Mehboob et al.[41] After testing $B_{12}N_{12}$ fullerenes for CO sensing capabilities, Beheshtian et al. found that $B_{12}N_{12}$ might be used as a CO sensor.[42]

There is an immense amount of research going on for the detection of gas molecules using nanomaterials. Kartika et al. examined the adsorption behaviour, electronic properties and sensitivity of mustard chemical warfare agent (CWA) on $Ca_{12}O_{12}$ nanocages by using density functional theory (DFT), revealing that $Ca_{12}O_{12}$ nanocages may be utilised to detect mustard gas.[43] The potential application of $Ca_{12}O_{12}$ nanocages as phosgene adsorption sensors was noted by Louis et al.[44] One more work

utilised DFT to examine the sensing characteristics of $Al_{12}Si_{12}$ after the adsorption of CH_4, CO, H_2, NO, and NH_3 gases.[45] After studying $Mg_{12}O_{12}$ nanocages coated with Zn, Hussain et al. found that they were effective in detecting $COCl_2$ gas.[46] Hussain et al. observed that $Mg_{12}O_{12}$ nanoclusters had enhanced adsorption properties for NO_2 gas after gold treatment.[47] Evidence from a density functional theory (DFT) investigation suggests that pure Al_6N_6 can detect CO, NO, and NH_3 gas molecules, while B_6N_6 can detect just NH_3 gas molecules properly.[48] Sainda et al. work on gas sensing and removal using Mg_9O_9 nanorings based on density functional theory.[49] Rahimi and Solimannejad worked on the CO2 capture and removal using B_6N_6 nanorings.[50] Patel et al. utilized C_{12}, B_6N_6 and Al_6N_6 nanorings for the sensing and detection of toxic gases using DFT.[48] Panchal et al. used AlN and BN nanorings to investigate their sensing performance for CO, NO and NH_3 hazardous gases.[51] Al-Otaibi et al. used a different type of nanoring for the sensing of the resorcinol molecule.[52] Al-Otaibi et al. also studied the sensing of cytosine on AlN, BN, and GaN nanorings using the solvent effect and the quantum theory of atoms in molecules.[53] To the best of our knowledge, no research has been conducted on the detection of SF_6 decomposed gases using AlN and BN nanorings.

Due to the need for real-time detection of SF_6 decomposition byproducts and the state of the art of 3D nanomaterials in gas sensing, this work explores the adsorption of SF_6 decomposed gases (H_2S, SO_2, SOF_2 and SO_2F_2) on AlN and BN nanorings based on density functional theory (DFT). Specifically, we will explore the structural and electronic properties of AlN and BN nanorings, along with the adsorption energy, charge transfer, and electronic behaviour of SF_6 decomposing gases on AlN and BN nanorings. We will assess the sensing capability of AlN and BN nanorings based on the change in electronic features following gas interactions. These key insights will lay the groundwork for the usability of AlN and BN nanorings as gas sensors to detect the presence of SF_6 decomposition, which is important for ensuring the reliability of electrical insulation systems and for minimizing potential environmental hazards.

2. Computational methods

Density functional theory (DFT) calculations were performed using the Gaussian 09 (ref. 54) program to assess the feasibility of utilizing AlN and BN nanoring for adsorbing SF_6 decomposed gases (H_2S, SO_2, SOF_2, SO_2F_2) during this work. GaussView 5.0 (ref. 55) was used for the designing of gases, nanocage, and all the complexes after the adsorption process. We used the widely-used B3LYP-D3 functional, which was chosen as an appropriate approach for studying the non-covalent interactions between interacting substances, along with 6-31G(d,p) basis set to compute the necessary data. Adding Grimme's D3 dispersion correction[56,57] approaches better for describing van der Waals interactions, which is important for the modelling of gas adsorption on AlN and BN nanoring. This approach predicts adsorption energy and charge transfer mechanism more reliably, resulting in a more accurate comprehensive gas-sensing analysis. To validate the structures at their local minima,

frequency calculations were performed after geometry optimization. Moreover, for the interaction between gases and the pristine nanocage, the adsorption energies (E_{ads}) were computed using eqn (1).[58]

$$E_{ads} = E_{complex} - (E_{nanocage} + E_{gas}) + BSSE \qquad (1)$$

where $E_{complex}$ is the energy of complex formed after the adsorption of gases on nanocage while $E_{nanocage}$ and E_{gas} are the total energy of monomers. To further test the acquired E_{ads} for basis set superposition error (BSSE), the counterpoise approach developed by Boys and Bernadi is used.[59] Furthermore, the energy gap (E_g) of the complex was computed using HOMO–LUMO data[60] to get more accurate results on the adsorption energies. The energy gap between HOMO and LUMO can be calculated using eqn (2).[61]

$$E_g = E_{LUMO} - E_{HOMO} \qquad (2)$$

In addition to obtaining and verifying the optimized structures through vibrational frequency calculations, the models in this work were examined for molecular electrostatic potential (MEP) levels, molecular orbital distribution patterns, density of states (DOS) results, and quantities of transferred charges (Q_T). The distribution of HOMO and LUMO orbitals was studied using the Multiwfn[57] and VMD[58] software packages. The data for density of states (DOS) was extracted using Multiwfn[62] and plotted using Origin[63] software. Furthermore, quantum theory of atoms in molecules (QTAIM) and non-covalent interactions (NCI) investigations were used to identify the interactions between the gas molecules and the nanocages. The sensor mechanism was evaluated using various parameters, including electrical conductivity, work function, recovery time, and sensing response. The minimal energy needed to release an electron from the sensor's Fermi level to a distance effectively remote from the surface is represented as work function (Φ).[64,65] The target gas may be detected when the Φ values change, which indicates a change in gate voltage that generates electrical signals.[66] The work function (Φ) value can be determined using eqn (3).[67]

$$\Phi = V_\infty - E_F \qquad (3)$$

E_F in the equation is Fermi level energy, which can be calculated using eqn (4).[68]

$$E_F = \frac{E_{HOMO} + E_{LUMO}}{2} \qquad (4)$$

3. Results and discussion

3.1 Optimization of geometry

Before conducting further computational analysis, geometry optimization represents a crucial step for optimizing the structure of the molecular systems and ensuring their structural stability.[69] In density functional theory (DFT) studies, performing a geometric optimization of molecules and nanostructures

allows one to find the most stable configuration, the closest to the minimum energy, as validation for further calculations, such as adsorption energies, charge transfer and other electronic properties.[70] In this study, the density functional theory (DFT) with the B3LYP-D3 functional and 6-31G(d,p) basis set was used to individually optimize all molecular systems (H_2S, SO_2, SOF_2, SO_2F_2, and AlN and BN nanorings). At the start, the H_2S, SO_2, SOF_2, and SO_2F_2 molecules were placed about 2.0 Å away from the closest atoms in the AlN and BN nanorings. As a result, the interactions evolved organically during optimization, without the need for hypothetical bond constraints. The gases are placed outside the AlN and BN nanorings to prepare eight distinct systems, which were also optimized using the functional mentioned above to obtain low-energy structures. The optimized geometries of all the systems under study are given in Fig. 1.

The bond lengths change from slight to significant by the adsorption of SF_6 decomposition gases H_2S, SO_2, SOF_2, and SO_2F_2 on AlN and BN nanorings as shown in Table 1. The bond length changes are indicative of the strength of interaction between the gas molecules and the nanorings. For AlN nanoring the largest shifts are observed in the SO_2F_2-out-AlN system where Al_1–N_{18} bond bumps from 1.705 Å to 1.829 Å and N_{18}–Al_{17} moves from 1.705 Å to 1.826 Å. The moderate shifts are to be found for SO_2-out-AlN where N_{18}–Al_1 moves from 1.705 Å to 1.774 Å and H_2S and SOF_2 adsorption exhibit only minor shifts ($\leq$0.02 Å). For BN nanoring, the bond lengths variations are not as sharp as AlN. The biggest variation is in SO_2-out-BN, with the bond B_3–N_4 growing from 1.315 Å to 1.321 Å and the other systems (H_2S, SOF_2, SO_2F_2) only show small shifts ($\sim$0.001–0.003 Å) in bond lengths. SO_2F_2 and SO_2 adsorption produce considerable charge redistribution, resulting in more robust interactions and higher structural distortion in AlN. Since BN nanoring is more covalent in nature, the charge transfer interactions are less strong, resulting in smaller fluctuations of bond lengths. Due to larger fluctuation of bond lengths in AlN nanoring than that in BN nanoring, AlN nanoring shows higher gas sensitivity than the latter.

3.2 Adsorption of SF_6 decomposed gases on AlN and BN

Herein, we report the interaction between AlN and BN nanorings with SF_6 decomposition gases using density functional theory (DFT). The sensing performance of these nanorings is evaluated based on the adsorption energy, charge transfer and geometry deviations. We also study the impact of electronic effects, adsorption strength and configurations of binding to identify the optimal nanoring for selective gas detection.

One of the most important parameters to characterize how strongly and how the gas adsorbs to the surface is the adsorption energy (E_{ads}). A higher negative adsorption energy with short interaction distance means a better interaction and is often attributed to chemisorption and a lower energy with long interaction distance is considered physisorption. The computed values of adsorption energy along with interaction distance are given in Table 2. The adsorption energy of SO_2F_2 is the highest at the value of -38.221 kcal mol^{-1} with lowest interaction
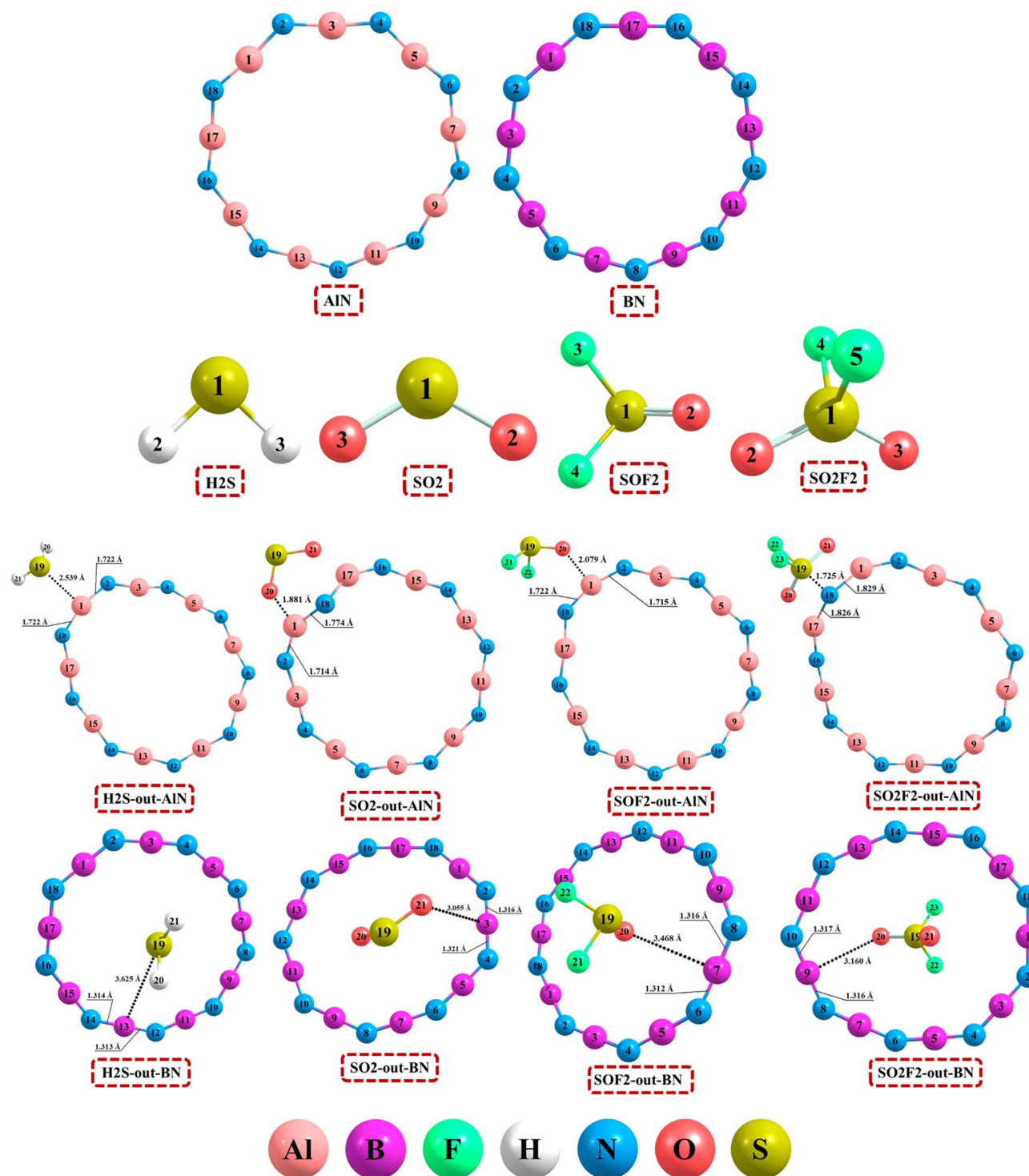
Fig. 1 The structure optimization of individual gases and nanorings along with all the systems after the adsorption process.

distance (1.725 Å) therefore indicating a strong chemisorption. The moderate interaction of SO$_2$ (−15.970 kcal mol^{-1}) at the interaction distance of 1.881 Å proposes a combined character of physisorption and chemisorption. Weak adsorption is observed for H$_2$S (−11.481 kcal mol^{-1}), and SOF$_2$ (−8.690 kcal mol^{-1}), indicating that the adsorption involves physical interaction (physisorption). Adsorption energies of BN

systems are however, lower than that of AlN, denoting weaker interactions. A range of −7.041 kcal mol^{-1} (H$_2$S) to −7.855 kcal mol^{-1} (SO$_2$F$_2$) is found, which is consistent with typical physisorption values. That means BN nanoring would have lower adsorption energies for SF$_6$ decomposition gases, in comparison with AlN. The calculated interaction distances for all BN cases are all greater than 3.0 Å, suggesting that

Table 1 The adsorption of SF_6 decomposed gases on AlN and BN results in the variations of bond lengths after the adsorption process

Systems	Connection	Bond lengths (Å)	
		Before	After
H_2S-out-AlN	Al_1–N_2	1.705	1.722
	N_{18}–Al_1	1.705	1.722
SO_2-out-AlN	Al_1–N_2	1.705	1.714
	N_{18}–Al_1	1.705	1.774
SOF_2-out-AlN	N_{18}–Al_1	1.705	1.722
	Al_1–N_2	1.705	1.715
SO_2F_2-out-AlN	Al_1–N_{18}	1.705	1.829
	N_{18}–Al_{17}	1.705	1.826
H_2S-out-BN	B_{13}–N_{14}	1.315	1.314
	N_{12}–B_{13}	1.315	1.313
SO_2-out-BN	B_3–N_4	1.315	1.321
	N_2–B_3	1.315	1.316
SOF_2-out-BN	B_7–N_8	1.315	1.316
	N_6–B_7	1.315	1.312
SO_2F_2-out-BN	B_9–N_8	1.315	1.316
	N_{10}–B_9	1.315	1.317

adsorption is predominantly dependent on weak van der Waals force (physisorption). It was found that H_2S has the lowest interaction distance (3.625 Å), which demonstrates the weak adsorption with BN nanoring.

Moreover, the charge transfer (Q_T) between the adsorbed gas molecules and the nanorings can help understand information about the adsorption phenomenon, and the potential of these materials as a sensor. Q_T are positive, suggesting the gas molecule electron donation to the nanoring, and Q_T are negative, corresponding to electron transfer from the nanoring to the gas molecule. It can be calculated using eqn (5).

$$Q_T = Q_{gas\ in\ complex} - Q_{gas} \qquad (5)$$

The SO_2 shows the highest degree of charge transfer, thus making it most electronically interactive with AlN as given in Table 2. Physisorption-dominated interactions are hinted by the electron donation from H_2S and SOF_2 to AlN. High adsorption energy of SO_2F_2 greatly leads to lower charge transfer, suggesting a more complex interaction mechanism. Low charge transfer values are consistent for BN systems with their physisorption on the surface for all gases. SOF_2 has the most charge

transfer to BN, but it is still weakly physisorbed. BN nanoring has the lower charge transfer, has intrinsic limits to its reactivity and is thus not suited for charge-based gas sensing.

3.3 Thermodynamics studies

The second law of thermodynamics states that chemical thermodynamics is the study of the heat-work connection as it pertains to chemical processes and physical state changes.[72,73] Thermodynamic variables, such as the enthalpy of formation (ΔH) and Gibbs free energy (ΔG) of a system, are crucial parameters that provide insight into the feasibility and spontaneity of adsorption reactions. These parameters allow us to know if the interaction between the SF_6 decomposition gases (H_2S, SO_2, SOF_2, SO_2F_2) and both nanorings (AlN and BN) is thermodynamically favourable and if the adsorption process occurs spontaneously. ΔH value of enthalpy of formation indicates the type of adsorption process, whether it is exothermic or endothermic. A negative ΔH indicates that the adsorption of these molecules is exothermic, thus promoting stability as energy is released following adsorption. Positive ΔH corresponds to endothermic adsorption, which requires energy input from outside and is generally less favourable. Gibbs free energy (ΔG) is used to assess whether the adsorption process is spontaneous or not. A negative ΔG indicates that the reaction can occur spontaneously and proceeds in a thermodynamically favourable direction. In thermodynamic terms, $\Delta G > 0$ is characteristic of a non-spontaneous reaction requiring external energy for adsorption to take place whereas ΔG equal to zero represents the equilibrium state of a reaction. Using the eqn (6)–(9), the enthalpy and Gibbs free energy values of the complexes were determined.

$$\Delta H° = \Sigma\Delta_f H° \text{product} - \Sigma\Delta_f H° \text{reactant (298.15 K)} \qquad (6)$$

$$\Delta_f H° = \Sigma(\varepsilon_o + H_{corr})\text{product} - \Sigma(\varepsilon_o + H_{corr})\text{reactant (298.15 K)} (7)$$

$$\Delta G° = \Sigma\Delta_r G° \text{product (298.15 K)} - \Sigma\Delta_r G° \text{reactant (298.15 K)} (8)$$

$$\Delta_r G° = \Sigma(\varepsilon_o + G_{corr})\text{product} - \Sigma(\varepsilon_o + G_{corr})\text{reactant (298.15 K)} (9)$$

here, ε_o stands for electronic energy, H_{corr} for thermal correction to enthalpy, and G_{corr} for thermal correction to Gibbs free energy. $D_f H°$ and $D_f G°$ are the standard enthalpy and Gibbs free

Table 2 The calculated values of adsorption energy (E_{ads}), distance of interaction (D), charge transfer (Q_T), changes in enthalpy (ΔH), and change in Gibbs free energy (ΔG)

Systems	E_{ads} (kcal mol^{-1})	D (Å)	BSSE (kcal mol^{-1})	E_{ads} past work	Q_T	ΔH	ΔG
H_2S-out-AlN	−11.481	2.539	1.638	−6.69 (ref. 71)	0.205	−11.458	−1.597
SO_2-out-AlN	−15.970	1.881	7.073	−8.53 (ref. 48)	−0.255	−22.524	−7.641
SOF_2-out-AlN	−8.690	2.079	5.502	−3.23 (ref. 48)	0.203	−13.315	5.143
SO_2F_2-out-AlN	−38.221	1.725	10.858	−3.46 (ref. 51)	−0.080	−47.862	−31.239
H_2S-out-BN	−7.041	3.625	1.581	−23.29 (ref. 51)	0.002	3.589	15.081
SO_2-out-BN	−7.549	3.055	5.099		0.024	−11.487	−1.391
SOF_2-out-BN	−7.294	3.468	7.948		0.059	−14.081	−3.901
SO_2F_2-out-BN	−7.855	3.160	6.071		0.045	−12.755	−2.120

energy of formation, respectively. Details on the system's enthalpy and Gibbs free energy are provided in Table 2, which is derived from density-functional theory (DFT) calculations conducted at a constant temperature of 298.15 K. The negative enthalpy of formation ($\Delta H < 0$) for H_2S, SO_2, SOF_2 and SO_2F_2 adsorption on AlN nanoring indicates that adsorption is an exothermic process and this type of process favours adsorption. Thus, the strongest interaction is found for SO_2F_2-out-AlN ($\Delta H = -47.86$ kcal mol^{-1}), denoting the most exothermic adsorption. The negative Gibbs free energy ($\Delta G < 0$) indicates that the adsorption process is spontaneous in most cases, except for SOF_2-out-AlN ($\Delta G = 5.14$ kcal mol^{-1}), which is a non-spontaneous process that would require external energy for adsorption to occur. Negative enthalpy values for BN systems (exothermic process) are consistent for SO_2, SOF_2, and SO_2F_2 systems, whereas H_2S-out-BN ($\Delta H = 3.58$ kcal mol^{-1}) is endothermic, which suggests weak or unstable interaction. As seen for SO_2, SOF_2 and SO_2F_2 the Gibbs free energy values are less than zero ($\Delta G < 0$) therefore all these adsorption processes are spontaneous while H_2S-out-BN ($\Delta G = 15.08$ kcal mol^{-1}) is non-spontaneous. Stronger and more spontaneous adsorption of SF_6 decomposition gases make the AlN nanoring a better candidate

for sensing. Although BN nanoring is effective, but it has less adsorption for H_2S, in particular.

3.4 Molecular orbital studies

Frontier Molecular Orbital (FMO) analysis is an important tool for elucidating the electronic properties and reactivity of materials. Highest occupied molecular orbital (HOMO) and lowest unoccupied molecular orbital (LUMO) are believed to be the contributing factor to study the electronic behaviour, chemical stabilization, and sensing capability of nanomaterials. Energy gap (E_g) is an important parameter that governs the electrical conductivity and chemical reactivity of a system. Systems with small energy gap show higher reactivity, good conductivity, and sensing ability. Through FMO analysis we can evaluate the impact on the electronic properties of AlN and BN nanorings from the adsorption of SF_6 decomposition gases. The decrease in energy gap following gas adsorption indicates improved electrical conductivity which makes it useful for sensor development as given in Table 3. The energy gap measurement of 3.690 eV for pure AlN reveals its moderate semiconducting properties. The adsorption of SO_2 on AlN nanoring results in a deep reduction of the energy gap to 1.103 eV from its initial state, showing a -70.115% decrease and leading to improved electrical conductivity. The adsorption of SOF_2 causes a minor energy gap reduction of -8.303% which points to a moderate level of electronic interaction. The slight increase in energy gap (1.578%) from SO_2F_2 adsorption demonstrates that AlN has only weak interaction with the nanoring which reduces its sensitivity to SO_2F_2 detection. The energy gap of pristine BN measures 6.267 eV which demonstrates its strong insulating properties. SO_2 adsorption creates a drastic decrease in the energy gap by 2.883 eV which represents a -54.006% reduction showing strong interaction capabilities that enhance sensing functions. The adsorption of SOF_2 results in a moderate -20.786% reduction of the energy gap which shows electronic structural changes. The change in energy gap after gas adsorption demonstrates AlN and BN

Table 3 The results of HOMO, LUMO, energy gap (E_g), percentage change of energy gap (% ΔE_g) and fermi energy (E_F) for all the systems under study

Systems	HOMO (eV)	LUMO (eV)	E_g	% ΔE_g	E_F
AlN	−6.556	−2.866	3.690	—	−4.711
H_2S-out-AlN	−6.120	−2.629	3.492	−5.383	−4.375
SO_2-out-AlN	−6.401	−5.298	1.103	−70.115	−5.849
SOF_2-out-AlN	−5.984	−2.600	3.384	−8.303	−4.292
SO_2F_2-out-AlN	−6.555	−2.806	3.748	1.578	−4.680
BN	−7.385	−1.115	6.269	—	−4.250
H_2S-out-BN	−7.319	−1.052	6.267	−0.039	−4.186
SO_2-out-BN	−7.252	−4.369	2.883	−54.006	−5.810
SOF_2-out-BN	−7.309	−2.343	4.966	−20.786	−4.826
SO_2F_2-out-BN	−7.355	−1.783	5.572	−11.115	−4.569
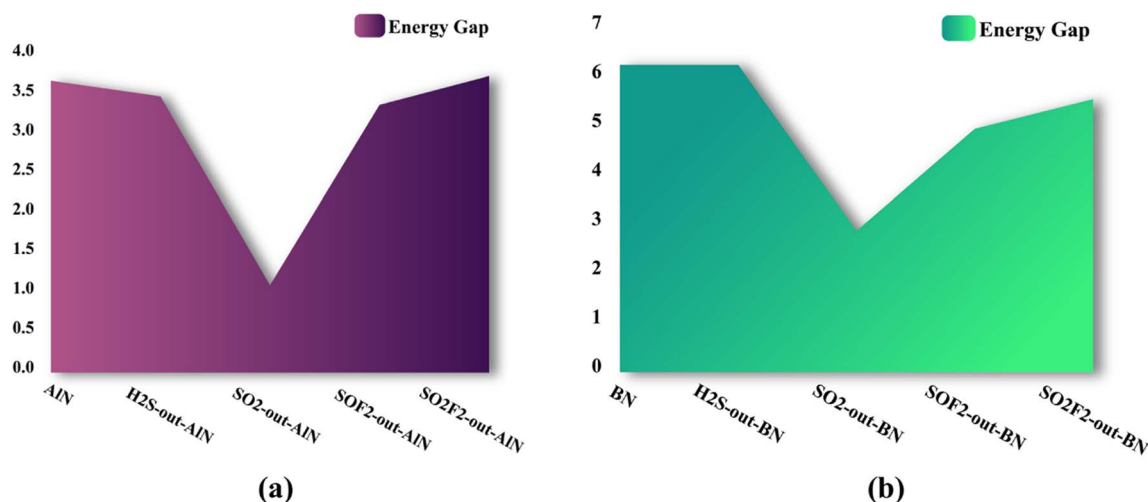
Fig. 2 The variations of energy gap (E_g) for (a) AlN based systems and (b) BN based systems.

nanorings as effective sensing materials. The change of energy gap is in Fig. 2(a) for AlN systems and Fig. 2(b) for BN systems. SO$_2$ adsorption on AlN and BN nanorings causes the greatest reduction in the energy gap which demonstrates their outstanding sensitivity for SO$_2$ detection. Both AlN and BN nanorings demonstrate significant responsiveness to SO$_2$ which
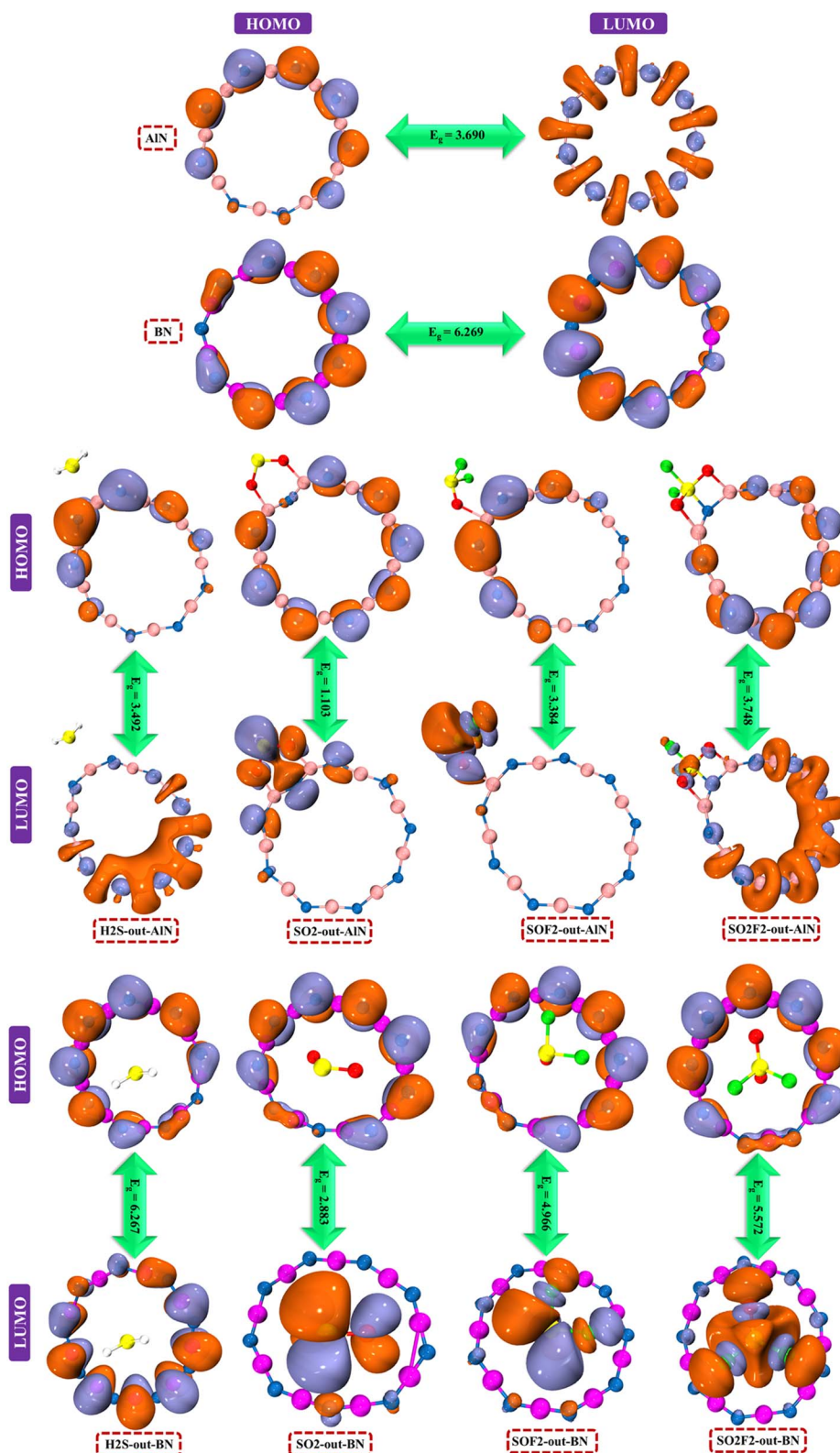

Fig. 3 The distribution of molecular orbitals (HOMO and LUMO) before and after the adsorption of SF$_6$ decomposed gases on AlN and BN nanorings.

establishes them as prime materials for SO_2 detection. Moreover, the adsorption of SO_2 and SOF_2 on AlN results in complete shift of LUMO orbitals on the surface of the gases due to the strong interaction between them and AlN nanoring as given in Fig. 3. Similarly, LUMO is also located on the surface of the gases after the adsorption of SO_2, SOF_2 and SO_2F_2 on BN nanoring. This redistribution of molecular orbitals after the adsorption process is indicative of electron transfer between analytes and nanorings.

3.5 Density of states (DOS)

The density of states (DOS) shows the number of possible energy levels for a given chemical system, making it an important statistic in solid physics. Its graph contains data that may be used to analyse the distribution of energy in molecular orbitals and the characteristics of electronic structure. Using the partial density of states (PDOS) and total density of states (TDOS), the quantum states in the studied nanostructured materials may be decomposed into the contributions from their respective atomic and molecular orbitals. The HOMO and LUMO energy states change at the Fermi level when SF_6 decomposed gases interact with the AlN and BN nanorings, as seen in Fig. 4. This occurs because of the orbital overlap taking place in the complexes under study.[74,75] The sensing capability of AlN and BN nanorings shifts due to changes in the Fermi level energy (E_F) resulting from gas adsorption, which signals electron transfer and density of states (DOS) adjustments as given in Table 3. The Fermi level of pristine AlN at -4.711 eV serves as a baseline for comparison studies. The interaction of H_2S with AlN nanorings causes the Fermi level (E_F) to increase to -4.375 eV through electron donation from the gas molecule, leading to a slight enhancement in conductivity. The Fermi level drops to -5.849 eV after SO_2 adsorption because the nanoring loses electrons to SO_2. The Fermi level energy (E_F) of pristine BN stands at -4.250 eV, which is higher than that of AlN showing that BN possesses more insulating characteristics. The adsorption of H_2S leads to a slight Fermi level change to -4.186 eV, which indicates limited electron transfer. SO_2 adsorption results in a significant Fermi level reduction to -5.810 eV, which replicates the effect observed on AlN. The Fermi level shows the weakest change when exposed to H_2S, which reveals a poor interaction and low sensing capability with both AlN and BN nanorings. The moderate shifts in SOF_2 and SO_2F_2 reveal weaker interactions compared to SO_2. The adsorption of SO_2 on AlN and BN produces the greatest downward Fermi level shift, which demonstrates their strong charge transfer properties and excellent sensing performance. SO_2 demonstrates the highest detectability in both AlN and BN nanorings because its strong electron-withdrawing properties produce significant Fermi level shifts. These results are consistent with what we observed in energy gap changes after the adsorption of SO_2 on both AlN and BN nanorings.

3.6 Electrostatic potential (ESP)

Understanding how molecular systems interact is made much easier with the help of the ESP. This method determines the molecule's size, shape, and locations of positive, negative, and neutral electrostatic potential. White, blue, and red are the
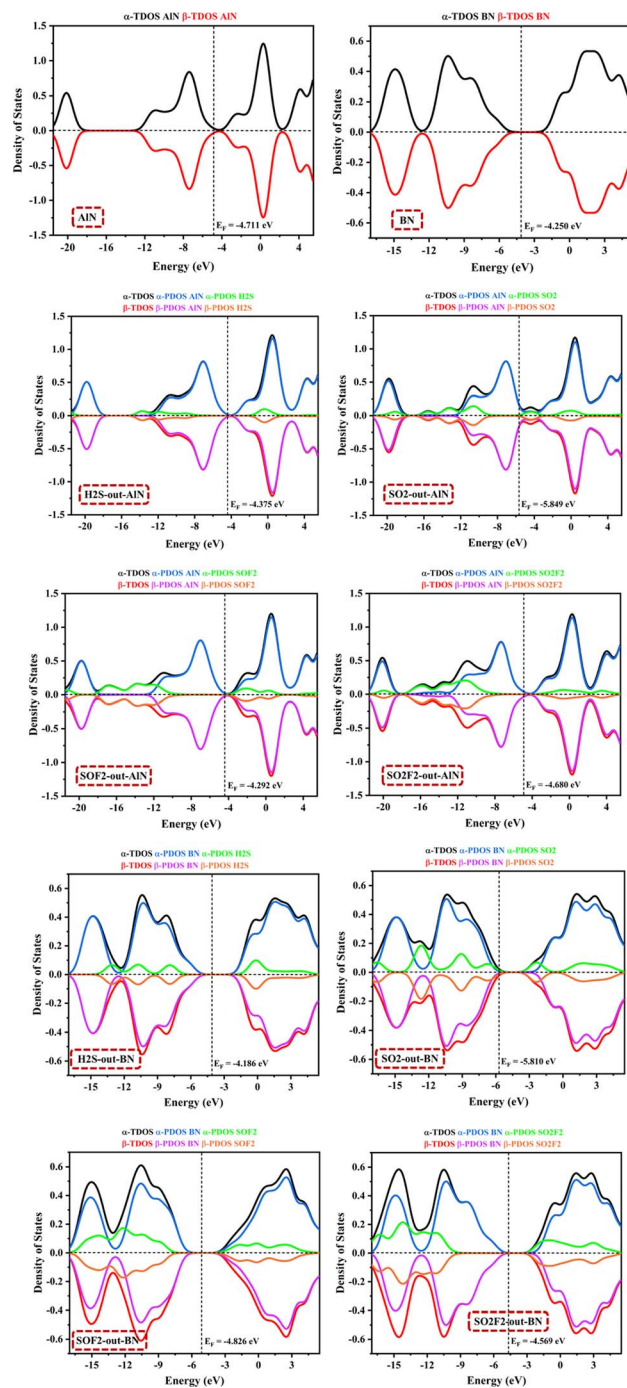
Fig. 4 The density of states (DOS) spectra for pure AlN, BN and all the systems after the adsorption of SF_6 decomposed gases.

colours shown on the MEP surface, which correspond to neutral, positive, and negative potential areas, respectively.[48,76,77] The AlN and BN nanorings have red regions in the centre and blue regions towards the outside ends, which represents their rich electron nature in the centre and electron deficient towards the ends as shown in Fig. 5. ESP results show that the adsorption of H_2S and SO_2F_2 gases on AlN results in a very little change of colours due to the minor charge transfer taking place between them according to Mulliken charge analysis (Q_T). This suggests that the

Fig. 5 Electrostatic potential (ESP) analysis showing the distribution of red, blue, and white areas on the surface of AlN, BN, and all the systems.

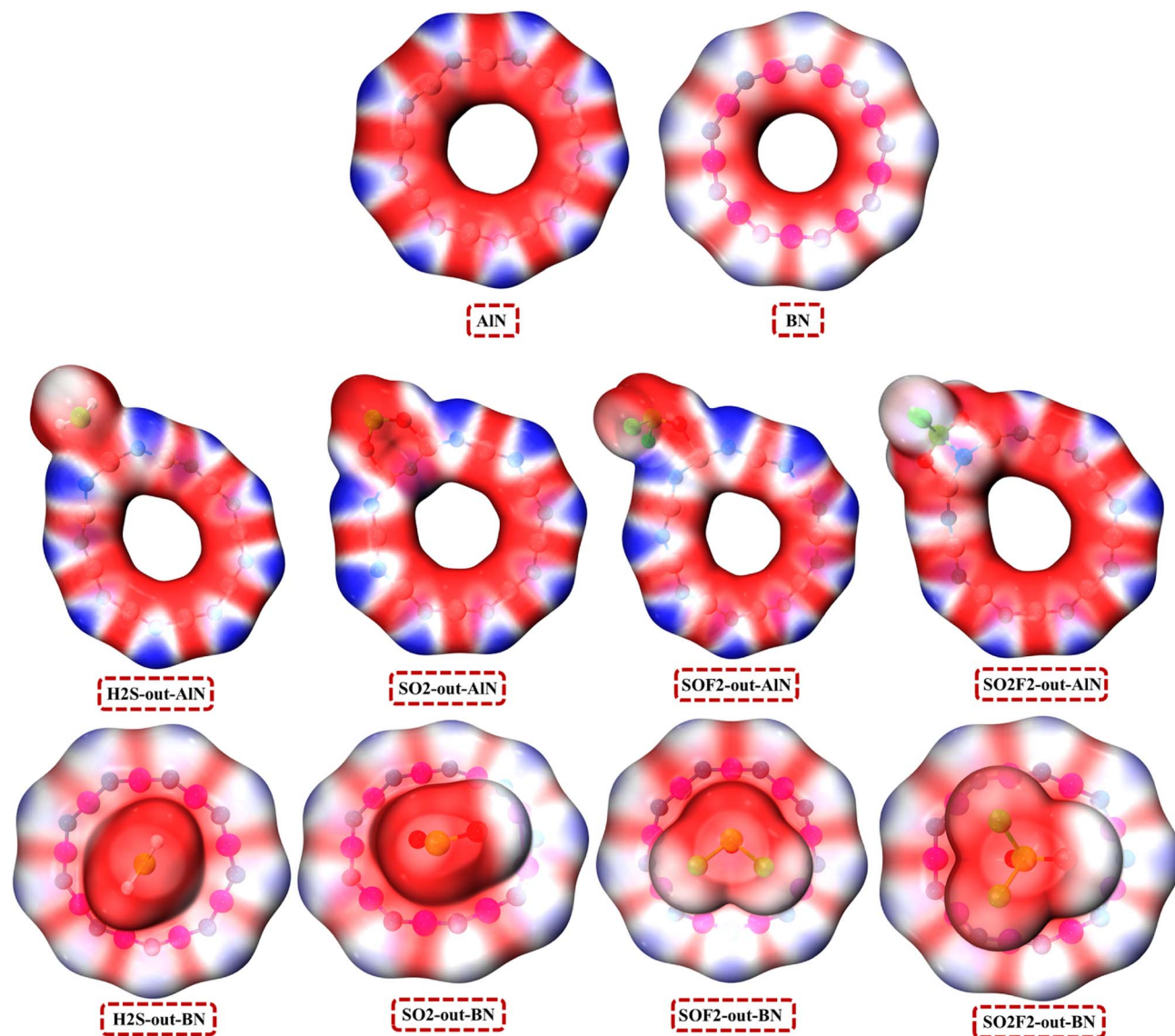physisorption nature of the interaction between these gas molecules and the AlN nanoring. In contrast, a chemisorption interaction and Mulliken charge analysis are confirmed by the red area of negative electrostatic potential over the SO_2 and SOF_2 gas molecules and the blue region of positive electrostatic potential on the nanoring as a consequence of SO_2 and SOF_2 gas molecule adsorption. As a result of SO_2 and SOF_2 gas molecules adsorption, the system's non-uniform distribution of atom charges generates various reactive sites. The adsorption of SF_6 decomposed gases on BN nanoring results in a more prominent distribution of red areas over the adsorbed gases. This suggests the electron donating nature of these gases towards the BN ring as confirmed by Mulliken charge analysis.

3.7 Chemical reactivity parameters

The stability and reactivity of SF_6 decomposed gases on the AlN and BN nanorings were investigated by calculating chemical reactivity parameters. The following parameters were identified by use of the B3LYP-D3/6-311(d,p) technique of density functional theory. Table 4 displays the anticipated chemical

Table 4 Chemical reactivity parameters including ionization potential (IP), electron affinity (EA), chemical hardness (η), chemical softness (σ), chemical potential (μ), and electrophilicity (ω)

Systems	IP	EA	σ	η	μ	ω
AlN	6.556	2.866	0.271	1.845	−4.711	6.014
H_2S-out-AlN	6.120	2.629	0.286	1.746	−4.375	5.481
SO_2-out-AlN	6.401	5.298	0.907	0.551	−5.849	31.026
SOF_2-out-AlN	5.984	2.600	0.296	1.692	−4.292	5.443
SO_2F_2-out-AlN	6.555	2.806	0.267	1.874	−4.680	5.844
BN	7.385	1.115	0.160	3.135	−4.250	2.881
H_2S-out-BN	7.319	1.052	0.160	3.133	−4.186	2.796
SO_2-out-BN	7.252	4.369	0.347	1.442	−5.810	11.708
SOF_2-out-BN	7.309	2.343	0.201	2.483	−4.826	4.690
SO_2F_2-out-BN	7.355	1.783	0.179	2.786	−4.569	3.747

hardness (η), chemical softness (σ), chemical potential (μ), and electrophilicity (ω) values for each complex. Eqn (10) and (11) of the extended Koopman's theorem provide the values of ionization potential (IP) and electron affinity (EA), respectively.

$$IP = -E_{HOMO} \tag{10}$$

$$EA = -E_{LUMO} \tag{11}$$

chemical hardness (η), chemical softness (σ), chemical potential (μ), and electrophilicity (ω) values are computed using eqn (12)–(15) respectively.

$$\eta = \frac{1}{2}(IP - EA) \tag{12}$$

$$\sigma = \frac{1}{2\eta} = \frac{1}{IP - EA} \tag{13}$$

$$\mu = -\frac{(I + A)}{2} \tag{14}$$

$$\omega = \frac{\mu^2}{2\eta} \tag{15}$$

According to data given in Table 4, there is a change in the values of chemical reactivity parameters after the adsorption process. BN exhibits greater chemical hardness (η) and stability compared to AlN based on their respective hardness values which are 3.135 eV for BN and 1.845 eV for AlN. Adsorption tends to decrease η values (with some exceptions) which results in complexes exhibiting higher reactivity compared to their pure surface counterparts. The lowest hardness for SO$_2$-out-AlN ($\eta = 0.551$ eV) and SO$_2$-out-BN ($\eta = 1.442$ eV) demonstrates that these interactions substantially modify the electronic stability of the nanorings. Since softness (σ) is calculated as the inverse of hardness, it demonstrates an opposite pattern of behaviour. The system SO$_2$-out-AlN and SO$_2$-out-BN demonstrates highest softness at 0.907 eV and 0.347 eV respectively, which denotes their increased polarizability and enhanced reactivity as compared to the remaining systems. More negative chemical potential (μ) values suggest stronger electron-attracting capability. The values -5.849 eV for SO$_2$-out-AlN and -5.810 eV for SO$_2$-out-BN represent the most negative μ values which demonstrate a stronger propensity to accept electrons and strong adsorption forces. Comparisons reveal only minor alterations in other complexes when matched against pure surfaces, which demonstrates intermediate interactions without severe changes in electronic structure. A system with higher ω values demonstrates stronger electrophilic characteristics, which leads to a greater electron acceptance tendency. The presence of SO$_2$ causes AlN ($\omega = 31.026$ eV) and BN ($\omega = 11.708$ eV) to become strong electrophiles compared to pure AlN ($\omega = 6.014$ eV) and BN ($\omega = 2.881$ eV) which indicates that these SO$_2$-treated systems attract electron-rich species more effectively. The limited increase in electrophilicity by other gases demonstrates their suitability for chemical sensing technologies. SO$_2$-out-AlN and SO$_2$-out-BN demonstrate major electronic
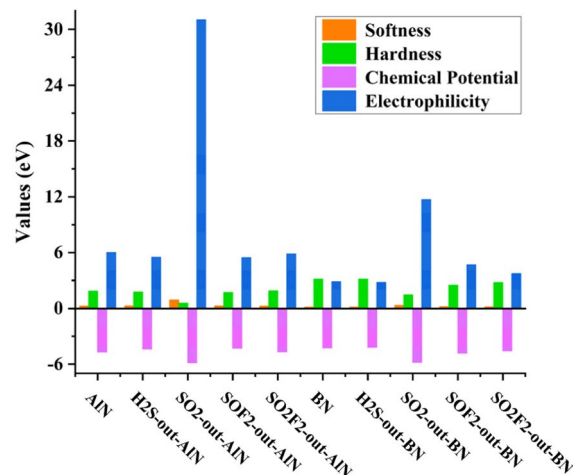

Fig. 6 Comparison between the different chemical reactivity parameters of all the systems including pristine AlN and BN nanorings.

changes which lead to their high softness and strong electrophilicity combined with low hardness thus creating highly reactive adsorption complexes. The softer and more reactive nature of AlN-based complexes makes AlN more suitable than BN-based complexes for adsorption-related applications. The variations between chemical hardness, chemical softness, chemical potential, and electrophilicity are given in Fig. 6.

3.8 Natural bond orbital (NBO) analysis

To verify the continued donor–acceptor orbital link between the adsorbed gases on the selected nanorings, we used natural bond orbital (NBO) analysis. It is an important method that shows how atomic species interact with each other and the distribution of electrons within molecular bonds.[78] The complex Schrödinger equation is reduced to the simpler level of chemical bonding using the NBO approach.[79] The investigation of the AlN and BN nanorings by NBO analysis reveals the delocalization of electrons and intermolecular charge transfer between the adsorbate gases. For NBO analysis, we used the B3LYP-D3/6-31G(d,p) method of density functional theory (DFT). One way to quantify the strength of the interaction between the orbitals of the donor and acceptor is by looking at the stabilization energy (E^2). The stabilization energies of the most interacting donor–acceptor orbitals in the systems that were studied are shown in Table 5. To calculate stabilization/perturbation energy, the following eqn (16) is used.

$$E^2 = \Delta E_{i,j} - q\frac{F^2(i,\ j)}{E(-E)} \tag{16}$$

In the equation E_i and E_j are the diagonal elements, $F(i,j)$ is the Fock Matrix, and q is the donor occupancy. The interactions between donor and acceptor orbitals are visualized in Fig. 7 for all the systems. SO$_2$F$_2$-out-AlN demonstrates the strongest interaction among studied complexes because the σ S$_{19}$–F$_{22}$ → σ^* N$_{18}$–S$_{19}$ transition produces a stabilization energy of 30.11 kcal mol^{-1}. The H$_2$S-out-AlN complex features a key

Table 5 The most prominent interactions between donor and acceptor orbitals of SF_6 decomposed gases and nanorings

Systems	Donor	Acceptor	E^2 kcal mol^{-1}	$E(j) - E(i)$ a.u.	$F(j, i)$ a.u.
H_2S-out-AlN	LP S_{19}	σ^* Al_1–N_2	9.38	0.69	0.073
	σ S_{19}–H_{20}	π^* Al_1–N_2	1.91	0.7	0.034
	π Al_1–N_2	σ^* S_{19}–H_{21}	0.18	0.43	0.008
SO_2-out-AlN	LP O_{20}	σ^* N_{18}–S_{19}	12.2	0.13	0.072
	π Al_{11}–N_{12}	π^* Al_{13}–N_{14}	17.02	0.29	0.063
	σ N_{14}–Al_{15}	σ^* N_{12}–Al_{13}	8.49	0.91	0.079
SOF_2-out-AlN	LP O_{20}	σ^* Al_1–N_{18}	9.06	0.72	0.074
	σ S_{19}–O_{20}	π^* Al_1–N_2	2.63	1.1	0.05
	π Al_1–N_2	σ^* S_{19}–O_{20}	0.48	0.43	0.013
SO_2F_2-out-AlN	σ S_{19}–F_{22}	σ^* N_{18}–S_{19}	30.11	1.06	0.16
	LP O_{20}	σ^* Al_{17}–O_{20}	28.92	0.67	0.125
	π Al_{13}–N_{14}	π^* Al_{15}–N_{16}	17.18	0.31	0.066
H_2S-out-BN	LP S_{19}	π^* B_9–N_{10}	0.98	0.38	0.018
	σ S_{19}–H_{20}	π^* B_{13}–N_{14}	0.23	0.68	0.012
	π B_{13}–N_{14}	σ^* S_{19}–H_{21}	0.07	0.52	0.006
SO_2-out-BN	LP O_{20}	π^* N_{12}–B_{13}	1.23	0.94	0.032
	σ S_{19}–O_{21}	π^* N_4–B_5	0.12	1.01	0.01
	π S_{19}–O_{21}	π^* N_4–B_5	0.54	0.61	0.017
SOF_2-out-BN	LP O_{20}	π^* N_8–B_9	0.5	0.45	0.014
	π S_{19}–O_{20}	π^* N_4–B_5	0.42	0.49	0.013
SO_2F_2-out-BN	LP O_{21}	π^* B_1–N_{18}	0.83	0.47	0.018
	π N_6–B_7	σ^* S_{19}–F_{23}	0.09	0.27	0.004

interaction between the lone pair (LP) of S_{19} and the anti-bonding σ orbital from the Al_1–N_2 bond that produces an E^2 energy value of 9.38 kcal mol^{-1}. Charge transfer between sulphur's lone pair and the anti-bonding orbital of the Al–N bond makes the Al–N bond weaker, which demonstrates moderate H_2S adsorption on AlN. A LP $O_{20} \rightarrow \sigma^*$ N_{18}–S_{19} interaction in SO_2-out-AlN delivers 12.20 kcal mol^{-1} of stabilization energy which demonstrates strong conjugation effects that improve the complex's electronic properties. The oxygen lone pair (LP O_{20}) transfers charge to the σ^* Al_1–N_{18} orbital and achieves 9.06 kcal mol^{-1} of stabilization energy in the SOF_2-out-AlN system revealing moderate interaction strength. BN-based complexes demonstrate weaker interactions in comparison to their AlN-based counterparts. SO_2-out-BN achieves the maximum stabilization energy for BN complexes through charge donation from LP O_{20} into the π^* N_{12}–B_{13} orbital with an E^2 energy value of 1.23 kcal mol^{-1}. The bonding shows low adsorption capability along with restricted electronic stabilization. The H_2S-out-BN complex features a lone pair (LP S_{19}) to π^* B_9–N_{10} transition which has E^2 value of 0.98 kcal mol^{-1} indicating minimal charge transfer. The observed stabilization energy in SOF_2-out-BN and SO_2F_2-out-BN is even weaker than other reported values, which suggests minimal interaction between BN and the adsorbed gases. The results show AlN-based systems possess stronger charge transfer interactions than BN-based systems, which makes AlN more appropriate for applications in gas adsorption and sensing. The SO_2F_2-out-AlN complex emerges as the most stable system because of its high stabilization energy which marks it as an excellent option for further study in gas sensing applications.

3.9 Atoms in molecules (AIM) analysis

Topological research was conducted using the atoms in molecules (AIM) analysis. Microelectronic and structural investigations alone may not be enough to decipher the complex system's intermolecular interactions. After the adsorption process AIM reveals information on the interactions between SF_6 decomposed gases and nanorings. This study examined various topological parameters, including total electronic density ($\rho(r)$), Laplacian of electron densities ($\nabla^2\rho(r)$), Lagrangian kinetic energy ($G(r)$), total electronic energy ($H(r)$), potential energy ($V(r)$), electron localisation function (ELF), and bond ellipticity (ε) at bond critical points (BCP). Bond critical point is a saddle point between two bonded atoms, which has the maximum electron density as shown in Fig. 8. Table 6 lists the topological features of the AlN and BN nanorings and how they interact with H_2S, SO_2, SOF_2 and SO_2F_2 gases at bond critical points (BCPs). Closed-shell interactions at a BCP are predicted by AIM theory when the total electron energy density (ρ) is positive. The presence of weak covalent contacts, also known as strong electrostatic interactions, occurs when $\nabla^2\rho > 0$ and $H > 0$, while the presence of a strong covalent bond occurs when $\nabla^2\rho < 0$ and $H < 0$. In contrast, a partial or medium covalent bond is indicated by $H < 0$ and $\nabla^2\rho > 0$. According to Table 6, all of the complexes that were tested had positive $\nabla^2\rho$ values and the majority of them had positive $H(r)$ values. Additionally, there exist a few negative $H(r)$ values. In other words, most of the bonds in our complexes are weak covalent interactions, while there are a few medium or partial covalent connections as well. Based on the literature study, mixed character interactions are present when the ratio of $V(r)$ to $G(r)$ is less than 2, but more than 1.[80] An indication of covalent bonding is when the value of $|V(r)|/G(r) > 2$ while the value of
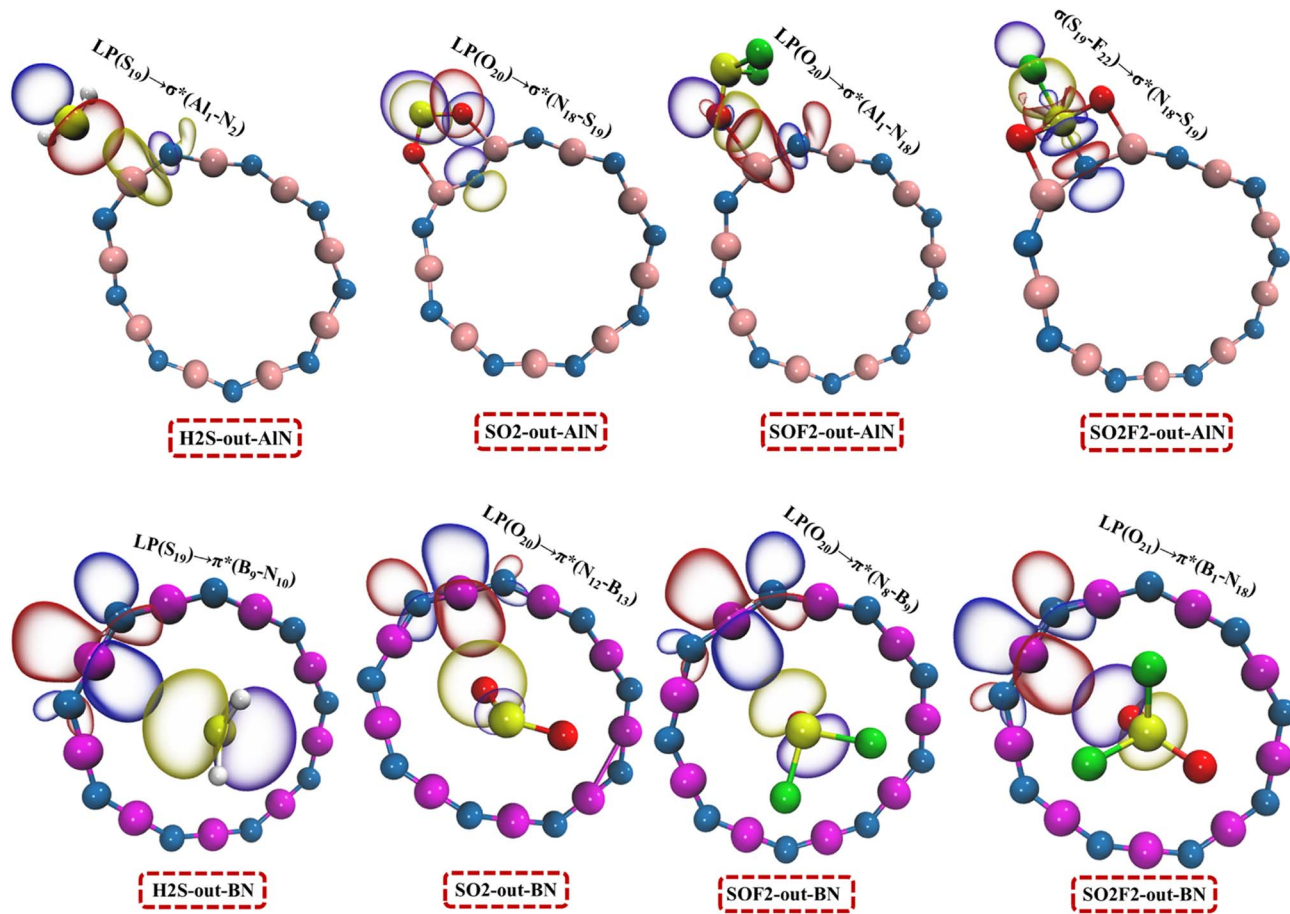
Fig. 7   Donor and acceptor interactions between natural bond orbitals (NBO) of AlN and BN-based systems.

$|V(r)|/G(r) < 1$ indicates ionic bonding and van der Waals interactions. The ratio of $V(r)$ to $G(r)$ is mostly less than 1 indicating van der Waals interactions between analytes and nanorings. Bond ellipticity (ε) is a significant measure for assessing interaction stability. When the value of ellipticity (ε) is less than 1, structural stability is suggested, whereas structural instability is indicated when the value of ellipticity is greater than 1. The bond ellipticity values are mostly less than 1 for AlN based systems while BN systems are mostly unstable due to higher ellipticity values. The delocalization of electronic density is studied using electron localization function (ELF) values. A number for ELF below 0.5 indicates that the electron is delocalised, whilst a value between 0.5 and 1 indicates that the electron is localised for bonding and non-bonding. Adsorption results in complexes with values less than 0.5, as seen in Table 6, suggesting that electrons have been delocalised in studied systems.

3.10   Non-covalent interactions (NCI)

NCI analysis functions as an effective computational method for displaying and analyzing weak intermolecular forces within molecular structures. Non-covalent interactions such as hydrogen bonding, van der Waals forces and dipole–dipole interactions stabilize molecular complexes unlike covalent bonds which involve strong electron sharing.[81] The Reduced Density Gradient (RDG) approach is the standard method used to carry out NCI analysis, which identifies spatial regions where non-covalent interactions happen.[82] The colours on the RDG map use blue to indicate strong attractive interactions like hydrogen bonding, while green represents weak van der Waals interactions and strong repulsive interactions from steric effects appear as red. The use of NCI analysis on our systems enables enhanced understanding of the non-covalent interactions between nanorings and gas molecules and verifies their stability and reactivity. The x-axis shows sign(λ_2)ρ which identifies various interaction types while the y-axis plots the Reduced Density Gradient (RDG) to detect interaction zones as shown in Fig. 9. In AlN based systems the strong blue regions (-0.020 to -0.050) provide evidence that hydrogen bonding and charge transfer interactions play major roles during adsorption. Green areas (near sign(λ_2)$\rho \approx 0$) of van der Waals interactions indicate that weak physisorption contributes to the stabilization of gas molecules upon the AlN surface. The red repulsive interactions demonstrate areas where steric hindrance blocks additional stabilization. The BN-based system displays weaker attractive forces because the blue regions show less intensity and fail to reach as far into negative values. The BN-based system displays a broader and stronger green region that indicates weak van der Waals interactions compared to the AlN-
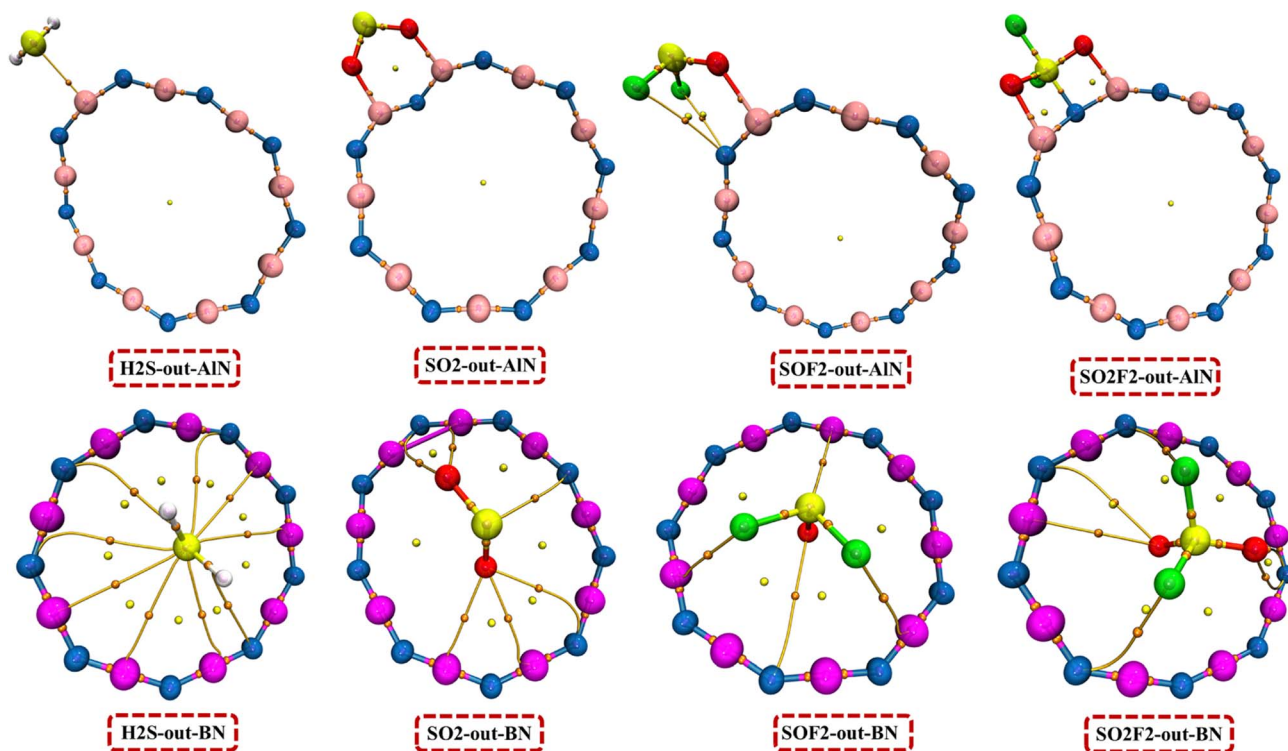
Fig. 8 Visual study of atom in molecules (AIM) analysis showing the important bond critical points (BCPs) between SF_6 decomposed gases and nanorings.

based system as also seen on their 3D iso-surface maps in Fig. 9. The reliance of BN-based systems on dispersion forces exceeds their dependence on strong electrostatic interactions and charge transfer mechanisms. The stronger attractive interactions from hydrogen bonding and charge transfer combined with reduced steric hindrance make AlN-based systems superior for gas adsorption. The analysis aligns with NBO findings because AlN systems demonstrate increased charge transfer stabilization while BN systems present reduced donor–acceptor interactions.

3.11 Sensing mechanism

The fundamental purpose for this study is to get a better understanding of the capability of AlN and BN nanorings to detect SF_6 decomposed gases. Various factors such as electrical conductivity (σ), sensing response (S), work function (Φ), and recovery time (τ) were assessed to achieve this goal.[83,84]

3.11.1 Electrical conductivity (σ). The gas sensor mechanism is better understood by comparing the electrical conductivity fluctuations of designed complexes before and after gas adsorption. For an electrical material to be electrically conductive, its capacity to transport electrons between the valence and conduction bands is critical.[85] Eqn (17), which involves examining the changes in energy gap both before and after gas adsorption, was used to compute the electrical conductivities of the complexes.

$$\sigma = AT^{3/2}\exp\left(\frac{-E_g}{2KT}\right) \qquad (17)$$

herein, A represents the Richardson constant 6×10^5 A m^{-2}, T is the working temperature (298 K), and k is Boltzmann constant (8.318×10^{-3} kJ mol^{-1} K^{-1}). The adsorption of SF_6 decomposed gases on nanorings results in the decrease of energy gap that increases the electrical conductivities as shown in Table 7. The variations between energy gap and electrical conductivity are given in Fig. 10(a). The conductivity of pure AlN nanoring reaches 3.77×10^{12} S m^{-1}. The electrical conductivity of the AlN system reaches its peak at 6.36×10^{12} S m^{-1} when modified with SO_2 to create the SO_2-out-AlN complex. The SOF_2-out-AlN complex shows improved conductivity with a value of 4.01×10^{12} S m^{-1} although it remains less conductive than the SO_2-out-AlN complex. The pure BN nanoring system demonstrates a conductivity level of 2.24×10^{12} S m^{-1}. The SO_2-out-BN complex shows maximum conductivity at 4.44×10^{12} S m^{-1} representing a major enhancement compared to pure BN which mirrors the behaviour found in AlN systems. The conductivity of the SOF_2-out-BN complex reaches 2.92×10^{12} S m^{-1} although it remains less impressive when compared to the SO_2-out-BN complex. SO_2 systems stand out as they display the highest conductivity levels among AlN and BN nanorings which positions them as top choices for high-conductivity applications. AlN-based systems typically demonstrate greater conductivity compared to BN-based systems, which suggests AlN as the superior choice for sensor applications.

3.11.2 Work function (Φ). The work function is defined as the minimum energy needed to remove an electron from the Fermi level (E_F).[86] The values of the work functions were obtained by using the eqn (3) and the changes in work function values are calculated using eqn (18).

Table 6 Different parameters of atoms in molecules (AIM) analysis performed for all the systems

BCP	Connection	$\rho(r)$	$\nabla^2\rho(r)$	$G(r)$	$V(r)$	$H(r)$	$V(r)/G(r)$	ELF	ε
H₂S-out-AlN									
34	Al_1–S_{19}	0.032	0.088	0.027	−0.033	−0.005	1.192	0.101	0.461
SO₂-out-AlN									
28	Al_1–O_{20}	0.058	0.429	0.098	−0.089	0.009	0.909	0.060	0.064
37	O_{21}–Al_{17}	0.058	0.429	0.098	−0.089	0.009	0.909	0.060	0.064
SOF₂-out-AlN									
32	N_{18}–F_{22}	0.007	0.029	0.006	−0.005	0.001	0.829	0.013	1.051
35	N_{18}–F_{21}	0.007	0.029	0.006	−0.005	0.001	0.828	0.013	1.162
42	Al_1–O_{20}	0.034	0.194	0.046	−0.044	0.002	0.949	0.049	0.331
SO₂F₂-out-AlN									
30	O_{20}–Al_{17}	0.066	0.458	0.110	−0.106	0.004	0.962	0.075	0.024
37	S_{19}–N_{18}	0.227	−0.509	0.093	−0.313	−0.220	3.369	0.871	0.063
43	O_{21}–Al_1	0.066	0.458	0.110	−0.106	0.004	0.962	0.074	0.026
H₂S-out-BN									
35	B_7–S_{19}	0.004	0.012	0.002	−0.002	0.001	0.696	0.016	5.243
43	S_{19}–B_{17}	0.004	0.012	0.002	−0.002	0.001	0.695	0.016	5.330
53	H_{20}–N_{12}	0.004	0.015	0.003	−0.002	0.001	0.618	0.009	2.303
SO₂-out-BN									
28	N_6–S_{19}	0.007	0.022	0.004	−0.003	0.001	0.726	0.029	0.936
37	B_3–O_{21}	0.007	0.025	0.005	−0.005	0.001	0.872	0.019	3.013
44	O_{20}–B_{13}	0.007	0.024	0.005	−0.005	0.001	0.867	0.017	3.181
SOF₂-out-BN									
30	B_{15}–F_{22}	0.006	0.026	0.005	−0.004	0.001	0.789	0.011	2.175
34	B_3–F_{21}	0.006	0.026	0.005	−0.004	0.001	0.790	0.011	2.165
45	S_{19}–B_9	0.004	0.017	0.003	−0.002	0.001	0.646	0.010	1.971
SO₂F₂-out-BN									
36	O_{20}–N_{10}	0.006	0.022	0.005	−0.004	0.001	0.821	0.014	4.388
56	N_4–F_{22}	0.005	0.025	0.005	−0.004	0.001	0.744	0.009	2.606
57	F_{23}–N_{16}	0.005	0.025	0.005	−0.004	0.001	0.745	0.009	2.534

$$\% \ \Delta\Phi = \frac{\Phi_{complex} - \Phi_{nanoring}}{\Phi_{nanoring}} \times 100 \tag{18}$$

here $\Phi_{complex}$ and $\Phi_{nanoring}$ are the work function values of complexes and pure nanorings. The molecular adsorption leads to substantial changes in work function as it demonstrates major electronic modifications to the nanoring surface as listed in Table 7. The work function measurement of pure AlN nanoring stands at 4.711 eV. The SO₂-out-AlN complex stands out among modified AlN systems by achieving the highest work function at 5.849 eV, which represents a 24.170% rise as compared to pure AlN. Investigation of the SOF₂-out-AlN and H₂S-out-AlN systems reveals decreased Φ values of 4.292 eV (−8.895%) and 4.375 eV (−7.139%), respectively, demonstrating a reduced electron attraction potential. The SO₂-out-BN complex demonstrates the highest Φ value at 5.810 eV, which represents the most substantial enhancement across all systems examined at 36.715% as compared to 4.250 eV of pure BN nanoring. The SOF₂-out-BN complex demonstrates a significant rise in Φ by 4.826 eV and 13.557% while the SO₂F₂-out-BN system shows a moderate Φ increase of 4.569 eV and 7.513%. The H₂S-out-BN complex shows a minor Φ decrease to 4.186 eV

with a −1.508% change that follows the same trend found in the AlN system. SO₂ complexes stand out as the top-performing systems for both AlN and BN nanorings because they demonstrate major enhancements in work function. SO₂ adsorption triggers substantial electronic modifications that position these complexes as top choices for electronic and sensor applications. The comparison of function for all the systems is given in Fig. 10(b).

3.11.3 Recovery time (τ) and effect of temperature. The bare minimum of time needed for a gas sensor to return to its initial form after gas sensing is known as recovery time (τ). More research on the reusability of nanomaterials is necessary due to the significant benefit of their low cost when used for gas sensing. The hypothetical study of recovery time for the adsorption of SF₆ decomposed gases on AlN and BN was conducted at two different temperatures. Eqn (19), in which E_{ads} is related to the recovery time, was used for the calculations of recovery time.[87]

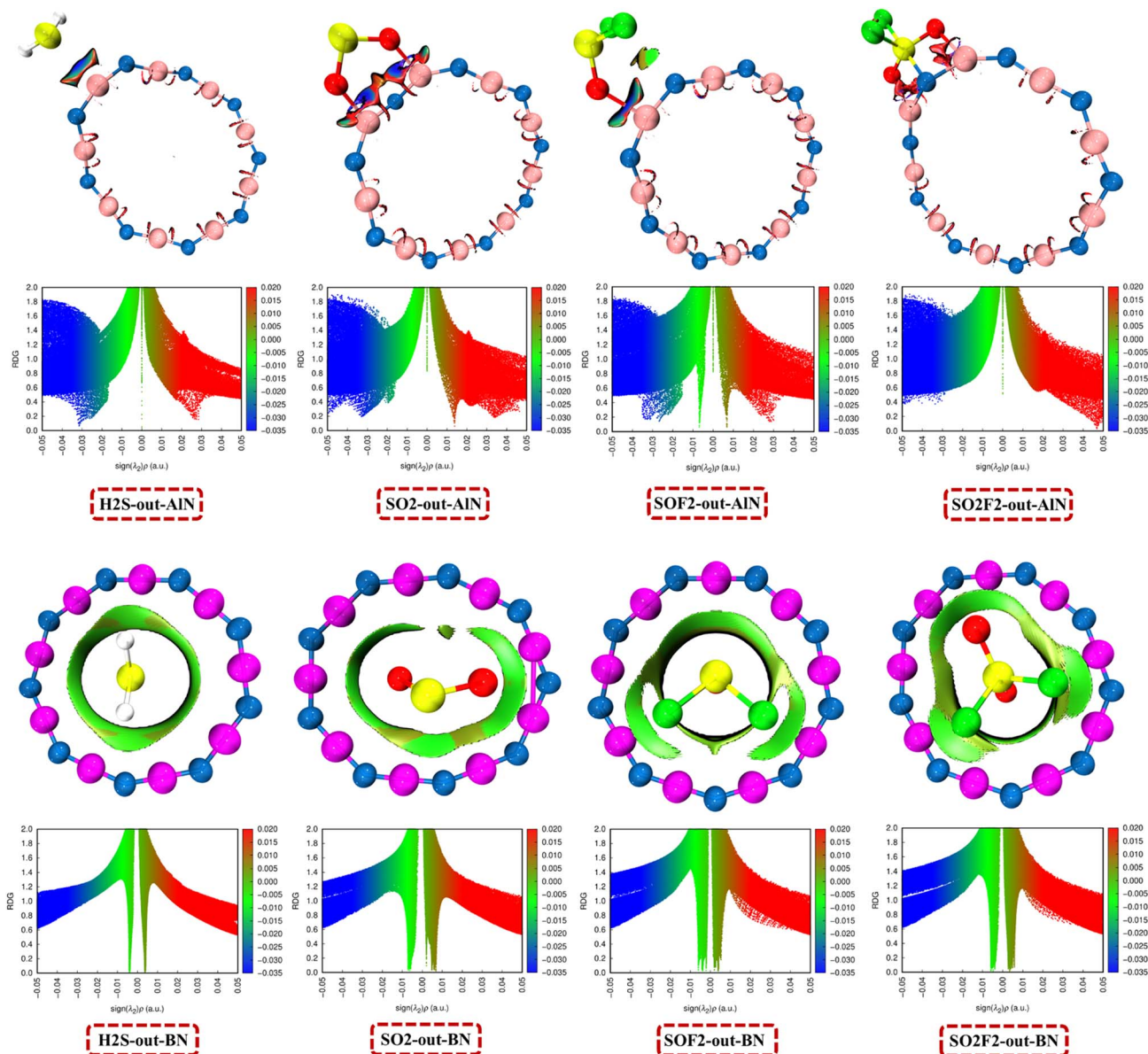$$\tau = V_o^{-1}\exp\left(\frac{-E_{ad}}{KT}\right) \tag{19}$$

Fig. 9 Reduced density gradient (RDG) maps and 3D iso-surfaces for the designed systems based on non-covalent interaction (NCI) studies.

In this equation, the variables V_o is the attempt frequency (10^{12} s^{-1}), E_{ads} is the adsorption energy, K is the Boltzmann constant, and T is the working temperature (298 K and 373 K). The results of recovery time at both these temperatures are given in Table 7. H$_2$S-out-BN achieves the fastest recovery from all systems with its shortest reaction time of 1.71×10^{-11} s.

Table 7 Values of electrical conductivity (σ), sensing response (S), work function (Φ), percentage change of work function (% $\Delta\Phi$) and recovery time (τ) for all the systems

| Systems	σ	Φ	% $\Delta\Phi$	τ (298 K)	τ (373 K)	S
AlN	3.77×10^{12}	4.711	—	—	—	—
H$_2$S-out-AlN	3.93×10^{12}	4.375	−7.139	1.03×10^{-10}	4.05×10^{-11}	0.0409
SO$_2$-out-AlN	6.36×10^{12}	5.849	24.170	6.28×10^{-10}	1.72×10^{-10}	0.6852
SOF$_2$-out-AlN	4.01×10^{12}	4.292	−8.895	3.33×10^{-11}	1.65×10^{-11}	0.0638
SO$_2$F$_2$-out-AlN	3.73×10^{12}	4.680	−0.647	4.97×10^{-6}	2.24×10^{-7}	−0.0117
BN	2.24×10^{12}	4.250	—	—	—	—
H$_2$S-out-BN	2.24×10^{12}	4.186	−1.508	1.71×10^{-11}	9.67×10^{-12}	0.0005
SO$_2$-out-BN	4.44×10^{12}	5.810	36.715	2.10×10^{-11}	1.14×10^{-11}	0.9797
SOF$_2$-out-BN	2.92×10^{12}	4.826	13.557	1.90×10^{-11}	1.05×10^{-11}	0.3006
SO$_2$F$_2$-out-BN	2.58×10^{12}	4.569	7.513	2.38×10^{-11}	1.26×10^{-11}	0.1509
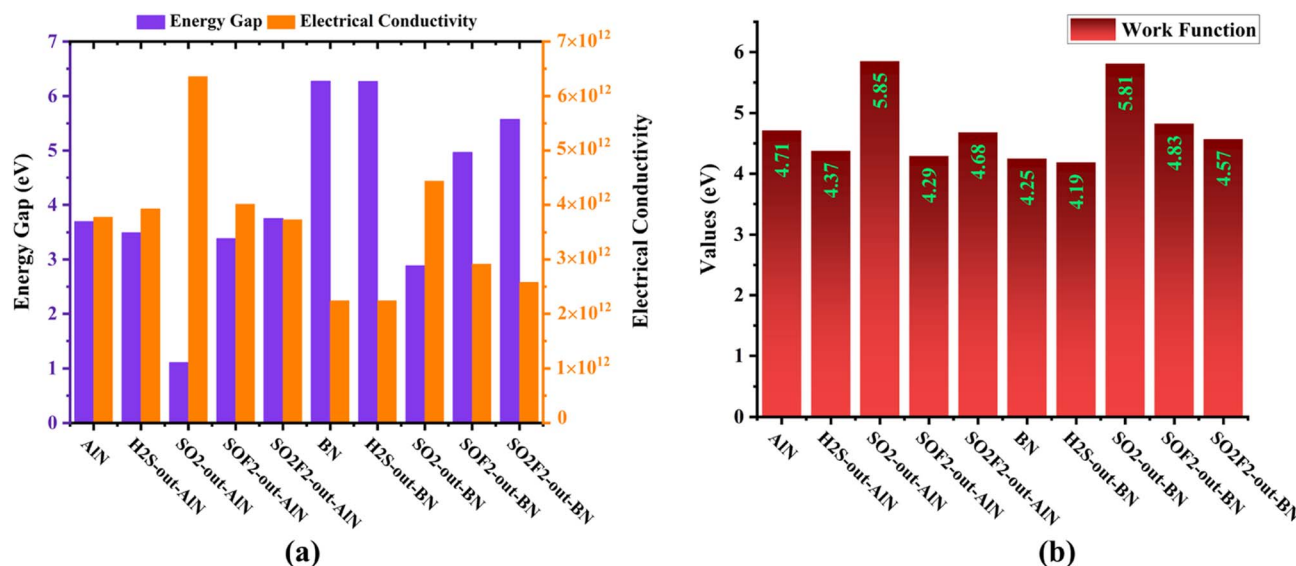
Fig. 10 Comparative study of (a) energy gap and electrical conductivity and (b) work function values of all the systems.

Both SOF$_2$-out-AlN (3.33 × 10^{-11} s) and SO$_2$-out-BN (2.10 × 10^{-11} s) systems display quick recovery times. The SO$_2$F$_2$-out-AlN system has the longest recovery time at 4.97 × 10^{-6} s which suggests slow sensor recovery and possible saturation challenges. All system recovery times decrease when temperatures rise from 298 K to 373 K and the most pronounced change is observed in SO$_2$F$_2$-out-AlN where RT reduces from 4.97 × 10^{-6} s to 2.24 × 10^{-7} s demonstrating that thermal energy speeds up desorption. H2S-out-BN shows minimal changes in recovery time because it already possesses very short RT at 298 K which demonstrates its natural efficiency in gas desorption even at room temperature. Gas sensors that need quick response and reset times perform best with BN-based systems since they demonstrate shorter RTs compared to AlN-based systems. The largest improvement in recovery times appears in SO$_2$F$_2$-out-AlN when temperatures increase.

3.11.4 Sensing response (S). The sensing response is a quantitative value that describes the degree of a surface to detect the adsorbed analyte molecules.[88,89] The sensing response is related to the electrical conductivity by the eqn (20).

$$S = \frac{\sigma_{\text{complex}}}{\sigma_{\text{nanocage}}} - 1 \qquad (20)$$

Gas sensor performance relies on sensitivity, which reflects the strength of the gas adsorption response. The maximum sensitivity of SO$_2$-out-BN at 0.9797 demonstrates an outstanding detection capability for SO$_2$ gas as shown in Table 7. AlN also demonstrates high sensitivity to SO$_2$ but performs less effectively compared to BN, which makes both materials suitable for SO$_2$ sensing with BN being the better option. The performance of SOF$_2$-out-BN at 0.3006 and SOF$_2$-out-AlN at 0.0638 is moderate but BN shows better results than AlN. Both nanorings show a poor performance in detecting H2S indicating that they are unsuitable for this application. SO$_2$F$_2$-out-AlN proves

unsuitable as a detection material because of its negative sensitivity.

4. Conclusion

Our research examined how Al$_9$N$_9$ (AlN) and B$_9$N$_9$ (BN) nanorings interact with different SF$_6$ decomposed gases such as H2S, SO$_2$, SOF$_2$ and SO$_2$F$_2$ through their adsorption behaviour and sensing abilities using density functional theory (DFT) calculations. We investigated several electronic and structural features such as adsorption energy (E_{ads}), energy gap (E_g), natural bond orbitals (NBO), chemical reactivity parameters, non-covalent interaction (NCI) analysis and sensing mechanism such as electrical conductivity, work function, recovery time, and sensitivity. Analysis of adsorption energy values demonstrates strong binding between AlN nanoring and both SO$_2$ and SO$_2$F$_2$ with adsorption energy values of −15.970 kcal mol^{-1} and −38.221 kcal mol^{-1} respectively, which indicates their high interaction stability as compared to BN based systems. Adsorption of SO$_2$ on both AlN and BN nanorings resulted in substantial band gap reductions in SO$_2$-out-AlN (−70.115%) and that SO$_2$-out-BN (−54.006%) as compared to pure AlN and BN nanorings. The reduction of energy gap caused improved electrical conductivity and sensor response during energy gap analysis. The NBO analysis validated substantial charge transfer within AlN based systems as compared to BN systems which amplified their adsorption-driven electronic structure changes. The systems with adsorbed molecules exhibited enhanced softness according to chemical reactivity parameter calculations while SO$_2$-out-BN (0.347 eV) and SO$_2$-out-AlN (0.907 eV) demonstrated the greatest softness increase which improved their reactivity and sensing application potential. The NCI analysis demonstrated that van der Waals forces and hydrogen bonding primarily govern interactions which lead to the stabilization of adsorbed complexes. The analysis revealed that SO$_2$

adsorption on BN nanoring (SO_2-out-BN) achieved the best results by displaying high sensitivity (0.9797) and substantial work function changes (36.715% increase), demonstrating its strong suitability for gas sensing devices. The SO_2-out-AlN system showed substantial changes in its electronic structure by achieving superior conductivity at 6.36×10^{12} S m^{-1} and a notable work function increase of 24.170%, positioning it as an excellent choice for gas sensor applications. The performance of a sensor heavily depends on recovery time, which defines how fast the sensor can revert to its original state following gas desorption. All the systems show fast recovery time with the fastest being reported for BN-based systems due to the weak adsorption of gases with BN nanoring. The raised temperature levels decreased recovery time, which validated thermal desorption as a feasible process. Our investigation identifies BN and AlN as good choices for SO_2 gas sensing applications because they provide strong adsorption properties alongside substantial electronic changes and improved conductivity while maintaining ideal recovery times. The research shows that BN and AlN nanorings function as highly effective materials for the detection of SF_6 decomposed gases with the superior performance of AlN nanoring based on better electrical conductivity, charge transfer and adsorption energy. This enables the use of AlN nanoring in environmental monitoring and industrial safety systems.

Data availability

The data are available from the corresponding author on reasonable request.

Author contributions

HAR contributed to the research design, writing of the original draft, investigation, validation, visualization, formal analysis, acquisition, and interpretation of data. MUK made a substantial contribution to the research design, conceptualization, methodology, project administration, investigation, data curation, supervision, review, and editing, and approval of the submitted version of the manuscript. AA had substantial contributions to the formal analysis, visualization, data curation, validation, writing, review & editing. SA had substantial contributions to the formal analysis, visualization, data curation, validation, funding, acquisition, writing, review & editing. MAA had a substantial contribution to the formal analysis, interpretation of data, validation, writing, review, and editing.

Conflicts of interest

The authors declare that they have no conflict of interest.

Acknowledgements

References

1 J. Chen, Q. Zhou, L. Jia, X. Cui and W. Zeng, The gas-sensing mechanism of Pt$_3$ cluster doped SnS$_2$ monolayer for SF$_6$ decomposition: a DFT study, *Appl. Surf. Sci.*, 2022, **597**, 153693.

2 L. Xu, Y. Gui, W. Li, Q. Li and X. Chen, Gas-sensing properties of Pt n-doped WSe$_2$ to SF$_6$ decomposition products, *J. Ind. Eng. Chem.*, 2021, **97**, 452–459.

3 Z. Liu, Y. Gui, L. Xu and X. Chen, Adsorption and sensing performances of transition metal (Ag, Pd, Pt, Rh, and Ru) modified WSe$_2$ monolayer upon SF$_6$ decomposition gases (SOF$_2$ and SO$_2$F$_2$), *Appl. Surf. Sci.*, 2022, **581**, 152365.

4 B. Li, Q. Zhou, R. Peng, Y. Liao and W. Zeng, Adsorption of SF$_6$ decomposition gases (H$_2$S, SO$_2$, SOF$_2$ and SO$_2$F$_2$) on Sc-doped MoS$_2$ surface: a DFT study, *Appl. Surf. Sci.*, 2021, **549**, 149271.

5 Y. Liao, Q. Zhou, R. Peng and W. Zeng, Adsorption properties of InP$_3$ monolayer toward SF$_6$ decomposed gases: a DFT study, *Phys. E*, 2021, **130**, 114689.

6 H. Cui, H. Zhu and P. Jia, Adsorption and sensing of SO$_2$ and SOF$_2$ molecule by Pt-doped HfSe$_2$ monolayer: a first-principles study, *Appl. Surf. Sci.*, 2020, **530**, 147242.

7 H. Liu, L. Xu, Y. Gui, L. Ran and X. Chen, Adsorption properties of Ag$_2$O–MoSe$_2$ towards SF$_6$ decomposed products, *Vacuum*, 2021, **189**, 110248.

8 A. Dong and M. Liu, A DFT study on the adsorption properties of Ti$_3$C$_2$O$_2$ MXene towards SF$_6$ decomposition gases, *Surf. Sci.*, 2023, **734**, 122317.

9 M. Istad and M. Runde, Thirty-six years of service experience with a national population of gas-insulated substations, *IEEE Trans. Power Delivery*, 2010, **25**(4), 2448–2454.

10 L. G. Christophorou, J. K. Olthoff and R. J. Van Brunt, Sulfur hexafluoride and the electric power industry, *IEEE Electrical Insulation Magazine*, 1997, **13**(5), 20–24.

11 O. Bender, H. J. Boehmer, D. Jens and K. P. Schumacher, Using GIS to analyse long-term cultural landscape change in Southern Germany, *Landscape and Urban Planning*, 2005, **70**(1–2), 111–125.

12 D. Chen, X. Zhang, J. Tang, Z. Cui and H. Cui, Pristine and Cu decorated hexagonal InN monolayer, a promising candidate to detect and scavenge SF$_6$ decompositions based on first-principle study, *J. Hazard. Mater.*, 2019, **363**, 346–357.

13 S. Rozas, R. Alcalde, M. Atilhan and S. Aparicio, A theoretical study on the adsorption of acid gases by boron nitride-based nanomaterials, *Appl. Surf. Sci.*, 2019, **480**, 83–95.

14 R. Geetha Sadasivan Nair, A. K. Narayanan Nair and S. Sun, Adsorption of Gases on Fullerene-like X$_{12}$Y$_{12}$ (X = Be, Mg, Ca, B, Al, Ga, C; Y = C, Si, N, P, O) Nanocages, *Energy Fuels*, 2023, **37**(18), 14053–14063.

15 S. Hussain, R. Hussain, M. Y. Mehboob, S. A. S. Chatha, A. I. Hussain, A. Umar, *et al.*, Adsorption of phosgene gas on pristine and copper-decorated B$_{12}$N$_{12}$ nanocages: a comparative DFT study, *ACS Omega*, 2020, **5**(13), 7641–7650.

16 R. G. S. Nair, A. K. N. Nair and S. Sun, Adsorption of gases on $B_{12}N_{12}$ and $Al_{12}N_{12}$ nanocages, *New J. Chem.*, 2024, **48**(18), 8093–8105.

17 F. S. Ghoreishi, A. Mahmoudi and S. M. Dehaghi, DFT insights into the electronic properties and gas sensing performance of $C_{19}X$ (X = C, N, and Si) nanocages for the detection of CO_2, CO, N_2, and H_2 gases, *Diamond Relat. Mater.*, 2024, **148**, 111348.

18 J. Shi, Y. Zhu, X. Zhang, W. R. G. Baeyens and A. M. García-Campaña, Recent developments in nanomaterial optical sensors, *TrAC, Trends Anal. Chem.*, 2004, **23**(5), 351–360.

19 J. Wang, Y. Chen and W. J. Blau, Carbon nanotubes and nanotube composites for nonlinear optical devices, *J. Mater. Chem.*, 2009, **19**(40), 7425–7443.

20 Z.-Y. Zhou, N. Tian, J.-T. Li, I. Broadwell and S.-G. Sun, Nanomaterials of high surface energy with exceptional properties in catalysis and energy storage, *Chem. Soc. Rev.*, 2011, **40**(7), 4167–4185.

21 C. Zhu, G. Yang, H. Li, D. Du and Y. Lin, Electrochemical Sensors and Biosensors Based on Nanomaterials and Nanostructures, *Anal. Chem.*, 2015, **87**(1), 230–249.

22 K. Yang, L. Zhu and B. Xing, Adsorption of Polycyclic Aromatic Hydrocarbons by Carbon Nanomaterials, *Environ. Sci. Technol.*, 2006, **40**(6), 1855–1861.

23 D. F. Emerich and C. G. Thanos, Nanotechnology and medicine, *Expet Opin. Biol. Ther.*, 2003, **3**(4), 655–663.

24 A. Kamyshny and S. Magdassi, Conductive Nanomaterials for Printed Electronics, *Small*, 2014, **10**(17), 3515–3535.

25 H. W. Kroto, J. R. Heath, S. C. O'Brien, R. F. Curl and R. E. Smalley, C60: Buckminsterfullerene, *Nature*, 1985, **318**(6042), 162–163.

26 J. Liu, A. G. Rinzler, H. Dai, J. H. Hafner, R. K. Bradley, P. J. Boul, *et al.*, Fullerene Pipes, *Science*, 1998, **280**(5367), 1253–1256.

27 M. L. Terranova, S. Orlanducci and M. Rossi, *Carbon Nanomaterials for Gas Adsorption*, CRC Press, 2012.

28 D. J. Babu, D. Puthusseri, F. G. Kühl, S. Okeil, M. Bruns, M. Hampe, *et al.*, SO_2 gas adsorption on carbon nanomaterials: a comparative study, *Beilstein J. Nanotechnol.*, 2018, **9**(1), 1782–1792.

29 R. Wang, D. Zhang, W. Sun, Z. Han and C. Liu, A novel aluminum-doped carbon nanotubes sensor for carbon monoxide, *J. Mol. Struct.: THEOCHEM*, 2007, **806**(1–3), 93–97.

30 X. Jia, L. An and T. Chen, Adsorption of nitrogen oxides on Al-doped carbon nanotubes: the first principles study, *Adsorption*, 2020, **26**(4), 587–595.

31 W. Wang, Y. Zhang, C. Shen and Y. Chai, Adsorption of CO molecules on doped graphene: a first-principles study, *AIP Adv.*, 2016, **6**(2), 025317.

32 R. Gholizadeh and Y.-X. Yu, N_2O + CO reaction over Si-and Se-doped graphenes: an ab initio DFT study, *Appl. Surf. Sci.*, 2015, **357**, 1187–1195.

33 S. Kumar, M. Malhotra and H. Sharma, Adsorption of gas molecules on ultra-thin pristine and doped graphene nanoribbons, *Mater. Res. Express*, 2018, **5**(10), 105007.

34 T. C. Nguyen and M. T. Nguyen, First-principles Studies of CO_2 and NH_3 Gas Molecules Adsorbed on Graphene Nanoribbons, *VNU Journal of Science: Mathematics-Physics*, 2016, **32**(2), 15–21.

35 E. Salih and A. I. Ayesh, Enhancing the sensing performance of zigzag graphene nanoribbon to detect NO, NO_2, and NH_3 gases, *Sensors*, 2020, **20**(14), 3932.

36 S. F. Rastegar, A. A. Peyghan, H. R. Ghenaatian and N. L. Hadipour, NO_2 detection by nanosized AlN sheet in the presence of NH_3: DFT studies, *Appl. Surf. Sci.*, 2013, **274**, 217–220.

37 J. Beheshtian, Z. Bagheri, M. Kamfiroozi and A. Ahmadi, A theoretical study of CO adsorption on aluminum nitride nanotubes, *Struct. Chem.*, 2012, **23**, 653–657.

38 A. Ahmadi, J. Beheshtian and N. L. Hadipour, Interaction of NH_3 with aluminum nitride nanotube: electrostatic vs. covalent, *Phys. E*, 2011, **43**(9), 1717–1719.

39 Y. Li, Z. Zhou and J. Zhao, Transformation from chemisorption to physisorption with tube diameter and gas concentration: computational studies on NH_3 adsorption in BN nanotubes, *J. Chem. Phys.*, 2007, **127**(18), 184705.

40 H. Y. Ammar, H. M. Badran and K. M. Eid, TM-doped $B_{12}N_{12}$ nano-cage (TM = Mn, Fe) as a sensor for CO, NO, and NH_3 gases: a DFT and TD-DFT study, *Mater. Today Commun.*, 2020, **25**, 101681.

41 M. Y. Mehboob, F. Hussain, R. Hussain, S. Ali, Z. Irshad, M. Adnan, *et al.*, Designing of Inorganic $Al_{12}N_{12}$ Nanocluster with Fe, Co, Ni, Cu and Zn Metals for Efficient Hydrogen Storage Materials, *J. Comput. Biophys. Chem.*, 2021, **20**(04), 359–375.

42 J. Beheshtian, Z. Bagheri, M. Kamfiroozi and A. Ahmadi, Toxic CO detection by $B_{12}N_{12}$ nanocluster, *Microelectron. J.*, 2011, **42**(12), 1400–1403.

43 R. Kartika, F. H. Alsultany, A. Turki Jalil, M. Z. Mahmoud, M. N. Fenjan and H. Rajabzadeh, $Ca_{12}O_{12}$ nanocluster as highly sensitive material for the detection of hazardous mustard gas: density-functional theory, *Inorg. Chem. Commun.*, 2022, **137**, 109174.

44 H. Louis, I. O. Amodu, T. O. Unimuke, T. E. Gber, B. B. Isang and A. S. Adeyinka, Modeling of $Ca_{12}O_{12}$, $Mg_{12}O_{12}$, and $Al_{12}N_{12}$ nanostructured materials as sensors for phosgene (Cl_2CO), *Mater. Today Commun.*, 2022, **32**, 103946.

45 L.-K. Li, Y.-Q. Ma, K.-N. Li, W.-L. Xie and B. Huang, Structural and electronic properties of H_2, CO, CH_4, NO, and NH_3 adsorbed onto $Al_{12}Si_{12}$ nanocages using density functional theory, *Front. Chem.*, 2023, **11**, 1143951.

46 S. Hussain, S. A. S. Chatha, A. I. Hussain, R. Hussain, M. Yasir Mehboob, A. Mansha, *et al.*, A Theoretical Framework of Zinc-Decorated Inorganic $Mg_{12}O_{12}$ Nanoclusters for Efficient $COCl_2$ Adsorption: A Step Forward toward the Development of $COCl_2$ Sensing Materials, *ACS Omega*, 2021, **6**(30), 19435–19444.

47 S. Hussain, S. A. S. Chatha, A. I. Hussain, R. Hussain, M. Yasir Mehboob, A. Mansha, *et al.*, In Silico Designing of $Mg_{12}O_{12}$ Nanoclusters with a Late Transition Metal for NO_2 Adsorption: An Efficient Approach toward the Development of NO_2 Sensing Materials, *ACS Omega*, 2021, **6**(22), 14191–14199.

48 S. Patel, P. Patel, D. Chodvadiya, N. N. Som and P. K. Jha, Adsorption performance of C_{12}, B_6N_6 and Al_6N_6 nanoclusters towards hazardous gas molecules: a DFT investigation for gas sensing and removal application, *J. Mol. Liq.*, 2022, **352**, 118702.

49 R. Sainda, D. Chodvadiya and P. K. Jha, A DFT study of Mg_9O_9 nanoring for gas sensing and removal applications, *J. Mol. Liq.*, 2024, **397**, 124121.

50 R. Rahimi and M. Solimannejad, A study combining DFT and molecular dynamics simulations into the performance of B_6N_6 nanosheets for CO_2 capture and separation, *Appl. Phys. A: Mater. Sci. Process.*, 2023, **130**(1), 21.

51 J. Panchal, A. Gauswami, D. Chodvadiya, H. Jadeja and P. K. Jha, Adsorption performance of CO, NO and NH_3 hazardous gas molecules over B_9N_9 and Al_9N_9 nanorings: Acumen from density functional theory, *Mater. Chem. Phys.*, 2024, **311**, 128565.

52 J. S. Al-Otaibi, Y. S. Mary, Y. S. Mary, J. N. C. Mishma and A. Manikandan, Investigation of the adsorption and sensor properties of resorcinol (RSL) on X_9N_9 (X = Al, B, Ga, In) nanorings by DFT and QTAIM analysis with solvent effects, *J. Mol. Liq.*, 2024, **398**, 124285.

53 J. S. Al-Otaibi, Y. S. Mary, U. Jethava, B. Chakraborty and M. C. Gamberini, Examining the adsorption and sensing characteristics of cytosine (CTE) on Y_9N_9 (Y = Al, B, Ga) nanorings using solvent effects, DFT, AIM and SERS analyses, *Spectrochim. Acta, Part A*, 2025, **337**, 126148.

54 M. J. Frisch, *Gaussian09*, 2009, https://www.gaussian.com/.

55 R. Dennington, T. Keith and J. Millam, *GaussView, Version 5*, 2009.

56 S. Grimme, S. Ehrlich and L. Goerigk, Effect of the damping function in dispersion corrected density functional theory, *J. Comput. Chem.*, 2011, **32**(7), 1456–1465.

57 S. Grimme and M. Steinmetz, Effects of London dispersion correction in density functional theory on the structures of organic molecules in the gas phase, *Phys. Chem. Chem. Phys.*, 2013, **15**(38), 16031–16042.

58 H. Liu, F. Wang, K. Hu, T. Li and Y. Yan, Pd_4 cluster decorated SnO_2 nanowire for detecting characteristic gases in oil-immersed transformers: a theoretical and experimental study, *Appl. Surf. Sci.*, 2022, **590**, 153122.

59 S. F. Boys and F. Bernardi, The calculation of small molecular interactions by the differences of separate total energies. Some procedures with reduced errors, *Mol. Phys.*, 1970, **19**(4), 553–566.

60 J.-i. Aihara, Reduced HOMO–LUMO gap as an index of kinetic stability for polycyclic aromatic hydrocarbons, *J. Phys. Chem. A*, 1999, **103**(37), 7487–7495.

61 Z. Chen, X. Zhang, H. Xiong, D. Chen, H. Cheng, J. Tang, *et al.*, Dissolved gas analysis in transformer oil using Pt-doped WSe_2 monolayer based on first principles method, *IEEE Access*, 2019, **7**, 72012–72019.

62 T. Lu and F. Chen, Multiwfn: a multifunctional wavefunction analyzer, *J. Comput. Chem.*, 2012, **33**(5), 580–592.

63 *Origin V*, OriginLab Corporation, Northampton, MA, USA, 2018.

64 G. Korotcenkov and G. Korotcenkov, Sensing layers in work-function-type gas sensors, in *Handbook of Gas Sensor Materials: Properties, Advantages and Shortcomings for Applications Volume 1: Conventional Approaches*, 2013, pp. 377–388.

65 G. Halek, I. D. Baikie, H. Teterycz, P. Halek, P. Suchorska-Woźniak and K. Wiśniewski, Work function analysis of gas sensitive WO_3 layers with Pt doping, *Sens. Actuators, B*, 2013, **187**, 379–385.

66 P. Davydovskaya, A. Tawil and R. Pohle, Ethanol sensing with Cu-BTC Metal Organic Framework: mass sensitive, work function based and IR investigations, *Key Eng. Mater.*, 2014, **605**, 87–90.

67 F. Zhuang, G. Hao, R. Zhou, W. Lei, Y. Deng, X. Ye, *et al.*, Electric fields and strains effect on the electronic and optical properties of Zr_2CO_2/MoSSe van der Waals heterostructure, *Mater. Today Commun.*, 2022, **33**, 104295.

68 H. A. Rizwan, M. U. Khan, A. Anwar, M. Idrees and N. A. Siddiqui, A molecular modeling study of pristine and Li-doped $B_{16}N_{16}$ nanocages for sensing G-series nerve agents using DFT-D3, *J. Mol. Graphics Modell.*, 2025, **139**, 109069.

69 C. J. Cramer, *Essentials of Computational Chemistry: Theories and Models*, John Wiley & Sons, 2013.

70 F. Jensen, *Introduction to Computational Chemistry*, John Wiley & Sons, 2017.

71 S. Vadalkar, D. Chodvadiya, N. N. Som, K. N. Vyas, P. K. Jha and B. Chakraborty, An ab-initio study of the C18 nanocluster for hazardous gas sensor application, *ChemistrySelect*, 2022, **7**(3), e202103874.

72 T. O. Unimuke, H. Louis, E. A. Eno, E. C. Agwamba and A. S. Adeyinka, Meta-hybrid density functional theory prediction of the reactivity, stability, and IGM of azepane, oxepane, thiepane, and halogenated cycloheptane, *ACS Omega*, 2022, **7**(16), 13704–13720.

73 A. Mardiana-Idayu and S. B. Riffat, An experimental study on the performance of enthalpy recovery system for building applications, *Energy and Buildings*, 2011, **43**(9), 2533–2538.

74 V. Nagarajan, R. Bhuvaneswari and R. Chandiramouli, Interaction studies of propylene and butadiene on tricycle graphane nanosheet–a DFT outlook, *J. Mol. Graphics Modell.*, 2023, **121**, 108449.

75 M. S. Jyothi, V. Nagarajan and R. Chandiramouli, Chemisorption of atrazine and diuron molecules on γ-arsenene nanosheet-a first-principles study, *Chem. Phys. Lett.*, 2022, **794**, 139484.

76 M. A. Hossain, M. R. Hossain, M. K. Hossain, J. I. Khandaker, F. Ahmed, T. Ferdous, *et al.*, An ab initio study of the B_{35} boron nanocluster for application as atmospheric gas (NO, NO_2, N_2O, NH_3) sensor, *Chem. Phys. Lett.*, 2020, **754**, 137701.

77 M. Arjmandi, A. Arjmandi, M. Peyravi and A. K. Pirzaman, First-principles study of adsorption of XCN (X = F, Cl, and Br) on surfaces of polyaniline, *Russ. J. Phys. Chem. A*, 2020, **94**, 2148–2154.

78 J. A. Agwupuye, H. Louis, T. O. Unimuke, P. David, E. I. Ubana and Y. L. Moshood, Electronic structure investigation of the stability, reactivity, NBO analysis,

thermodynamics, and the nature of the interactions in methyl-substituted imidazolium-based ionic liquids, *J. Mol. Liq.*, 2021, **337**, 116458.

79 R. Gangadharan and S. Sampath Krishnan, Natural bond orbital (NBO) population analysis of 1-azanapthalene-8-ol, *Acta Phys. Pol. A*, 2014, **125**(1), 18–22.

80 H. A. Rizwan, M. U. Khan, A. Hamid, J. Yaqoob, R. Hussain, S. Ahmed, *et al.*, Molecular modelling of $Al_{24}N_{24}$ nanocage for the chemical sensing of phosgene and mustard chemical warfare agents: first theoretical framework, *Comput. Theor. Chem.*, 2023, **1230**, 114349.

81 E. R. Johnson, S. Keinan, P. Mori-Sánchez, J. Contreras-García, A. J. Cohen and W. Yang, Revealing Noncovalent Interactions, *J. Am. Chem. Soc.*, 2010, **132**(18), 6498–6506.

82 G. Saleh, C. Gatti and L. Lo Presti, Non-covalent interaction via the reduced density gradient: independent atom model vs. experimental multipolar electron densities, *Comput. Theor. Chem.*, 2012, **998**, 148–163.

83 M. M. Edim, O. C. Enudi, B. B. Asuquo, H. Louis, E. A. Bisong, J. A. Agwupuye, *et al.*, Aromaticity indices, electronic structural properties, and fuzzy atomic space investigations of naphthalene and its aza-derivatives, *Heliyon*, 2021, **7**(2), e06138.

84 V. Nagarajan and R. Chandiramouli, Sensing response of novel ε-antimonene nanosheet towards ethyl acetate and isopropyl acetate–a DFT insight, *Chem. Phys.*, 2022, **562**, 111632.

85 N. F. Mott, Conduction in non-crystalline materials: III. Localized states in a pseudogap and near extremities of conduction and valence bands, *Philos. Mag.*, 1969, **19**(160), 835–852.

86 J. Chen, G. Zhu, F. Wang, Y. Xu, C. Wang, Y. Zhu, *et al.*, Design of flexible strain sensor with both ultralow detection limit and wide sensing range via the multiple sensing mechanisms, *Compos. Sci. Technol.*, 2021, **213**, 108932.

87 V. Nagarajan, R. Ramesh and R. Chandiramouli, Chemical sensing properties of σ-PXene sheets towards dioxin vapours–a first-principles insight, *Comput. Theor. Chem.*, 2023, **1228**, 114300.

88 S. Saravanan, V. Nagarajan, A. Srivastava and R. Chandiramouli, Blue phosphorene nanoribbon for detection of chloroform vapours–a first-principles study, *Int. J. Environ. Anal. Chem.*, 2021, **101**(12), 1697–1709.

89 H. A. Rizwan, M. U. Khan, A. Anwar, M. U. Khan, A. Sohail, S. Ahmed, *et al.*, Deciphering the adsorption and sensing performance of $Al_{24}N_{24}$ and $B_{24}N_{24}$ nanoclusters as a drug delivery system for nitrosourea anticancer drug: a DFT insight, *Surf. Interfaces*, 2024, **51**, 104779.